J. Fluid Mech. (2005), *vol.* 544, *pp.* 201–241.
doi:10.1017/S0022112005006804 Printed in the United Kingdom

Investigation of the near-field tip vortex behind an oscillating wing

By D. BIRCH AND T. LEE

Department of Mechanical Engineering McGill University, Montreal, Quebec, Canada H3A 2K6

(Received 20 October 2004 and in revised form 16 June 2005)

The near-field tip-vortex flow structure behind an oscillating NACA 0015 wing was investigated at $Re = 1.86 \times 10^5$. For attached-flow and light-stall oscillations, a small hysteretic property existed between the pitch-up and pitch-down motion, and many of the vortex flow features were found to be qualitatively similar to those of a static wing. For deep-stall oscillations, the wing oscillations imposed a strong discrepancy in contour shapes and magnitudes between the pitch-up and pitch-down phases of the oscillation cycle. The vortex was less organized during pitch-down (as a result of leading-edge-vortex-induced massive flow separation) than during pitch-up. The tangential velocity, circulation and lift-induced drag increased progressively with the airfoil incidence, and had higher magnitudes during pitch-up than during pitch-down, while varying slightly with the downstream distance. The vortex size, however, was larger during pitch-down than during pitch-up. The axial flow was always wake-like during the deep-stall oscillation cycle. The normalized circulation within the inner region of the tip vortex also exhibited a self-similar structure, similar to that of a static wing, and was insensitive to the reduced frequency.

1. Introduction

The counter-rotating vortices generated by aircraft wing tips, because of their hazardous effects on flight safety and airport capacity, continue to be of concern to aviation industry and aircraft manufacturers alike. Of particular concern are the upsetting effects on aircraft landing at busy terminals where sufficient manoeuvring altitude may not be available to recover from the rolling or pitching motions induced by the vortices. Numerous experimental, theoretical and computational investigations have been conducted to improve the understanding of the tip vortex structure and its dissipation or persistence, as well as its control. However, unlike the usual lack of experimental data, a substantial effort has been invested in developing theoretical and numerical models for the roll-up process of tip vortices (for example, Hoffman & Joubert 1963; Batchlor 1964; Moore & Saffman 1973; Rossow 1973; Maskell 1973; Williams 1974; Crow 1979; Phillips 1981; Green & Acosta 1991; Mayer & Powell 1992; Brune 1994; Spalart 1998; Gerz & Holzapfel 1999). Nevertheless, the bulk of the experimental effort has been directed toward finding the rate of change of the tangential velocity and the strength of trailing vortices in the intermediate or far-field regions, while addressing the issues of vortex development, stability, and breakdown. Only limited investigations (Corsiglia, Schwind & Chigier 1973; Francis & Kennedy 1979; Francis & Katz 1988; Shekarriz *et al.* 1993; Devenport *et al.* 1996; Chow, Zilliac & Bradshaw 1997; Ramaprian & Zheng 1997; Birch & Lee 2004) have been conducted to investigate the dynamics of the initial rollup of a tip vortex around

the stationary wing tip, and to document the subsequent development of axial and tangential velocities and the turbulence structure with the downstream distance in the near field.

Among the representative near-field tip vortex investigations, Devenport *et al.* (1996) investigated the vortex structure in the range of $x/c = 4$ to 29 downstream of a NACA 0012 airfoil with a blunt tip and an aspect ratio AR of 4.33 at $Re = 5.3 \times 10^5$ by using a miniature four-sensor hot-wire probe mainly at $\alpha = 5^\circ$, and showed a deficit profile of approximately 84 % of the free-stream velocity. Also, the flow outside the core was dominated by the remainder of the wing wake which wound into an ever-increasing spiral, and the turbulence stress levels varied along the wake spiral in response to the varying rate of strain imposed by the vortex. Chow *et al.* (1997) investigated the tip vortex flow (up to $x/c = 0.678$) of a NACA 0012 airfoil model with a rounded tip and an AR of 1.333 at $Re = 4.6 \times 10^6$ and $\alpha = 10^\circ$ by using a seven-hole pressure probe and a triple-hot-wire probe, and indicated a high level of axial velocity excess of approximately $1.7u_\infty$ at all measurement locations. Chow *et al.* also reported that the turbulence in the vortex flow can be as high as 24 % r.m.s. velocity, and decayed quickly with streamwise distance because of the stabilizing effect of the nearly solid-body rotation of the vortex-core mean flow. Ramaprian & Zheng (1997) observed no axial velocity excess for a tip vortex generated by a rectangular, square-tipped NACA 0015 wing with $Re = 1.8 \times 10^5$ at $\alpha = 10^\circ$ up to $x/c = 3.3$ by using a three-component laser Doppler anemometer. The inner part of the three-dimensional vortex was, however, found to be nearly axisymmetric within $x/c = 2.0$ and exhibited a universal structure of conceptual asymptotic trailing vortices. Recently, Birch & Lee (2004) examined the flow structure both along the tip and in the near field (up to $x/c = 2.5$) behind a square-tipped, rectangular NACA 0015 wing at $Re = 2.1 \times 10^5$ for $\alpha = 2^\circ$ to 19° by using a miniature seven-hole pressure probe and a triple-hot-wire probe. The circulation was observed to have a local maximum at $x/c, = 0.05$ and remained virtually unchanged up to $x/c = 2.5$. The vortex flow was also self-similar and axisymmetric for $x/c \geqslant 0.5$. The lift-induced drag was also computed and compared with the wind-tunnel force-balance data.

On the other hand, it is noteworthy that the near-field behaviour of a tip vortex is also of particular importance in rotary wing aerodynamics. Tip vortices shed from helicopter rotor blades and propellers interact with following blades, causing rotor-blade–vortex-interaction (BVI) noise and vibration. The near-field flow characteristics of a tip vortex thus play a significant role in the understanding and control of BVI noise and vibration of rotorcraft, and are directly affected by the dynamic-stall flow phenomena occurring on the retreating blades of a helicopter. The phenomenon of dynamic stall on airfoils and lifting surfaces in unsteady flow environments has been recognized and studied for many years, both as an important practical problem and as a challenging fundamental one as well. Extensive experimental and computational investigations (for example, Johnson & Ham 1972; McCroskey & Philippe 1975; Carr, McAlister & McCroskey 1977; McCroskey *et al.* 1981; McCroskey, Carr & McAlister 1976; Jumper, Dimmick & Alliare 1989; Ericsson & Reding 1988; Chandrasekhara & Carr 1990; Srinivassan, Ekaterinaris & McCroskey 1993; Schreck, Faller & Hellin 1994; Panda & Zaman 1994; Ko & McCroskey 1997; Lee & Basu 1998; Lee & Gerontakos 2004) have been conducted to investigate the dynamic-stall flow events developed on an unsteady airfoil. It is now known that the predominant feature of dynamic stall is the formation, convection and shedding over the upper surface of the airfoil of a leading-edge vortex (LEV), or dynamic-stall vortex (DSV), which induces a nonlinearly fluctuating pressure field and produces

large transient variations in forces and moments that are fundamentally different from their steady-state counterparts. After the energetic LEV passes off the trailing edge, the flow progresses to a state of full separation over the upper surface, and is accompanied by a sudden loss of lift and increase in the negative pitching moment. Furthermore, if α becomes low enough, the flow will finally reattach again from the leading edge. An excellent review is given by McCroskey (1982). Most recently, the spatial–temporal progression of the critical boundary-layer flow points (including transition, flow reversal and separation, and reattachment and relaminarization), and also the behaviour of the LEV were measured and characterized non-intrusively Lee & Basu (1998) and Lee & Gerontakos (2004) by using closely spaced multiple-hot-film sensor (MHFS) arrays, in conjunction with surface pressure measurements.

Lee and coworkers reported that for a NACA 0012 airfoil (hinged at the $\frac{1}{4}$-chord location) subjected to deep-stall oscillations, the prior-to-stall boundary-layer conditions were dominated by the approximately linear forward spread of a trailing-edge turbulent flow reversal (always up to an uppermost position of $s/c = 0.26$; s is the surface distance from the leading edge of the airfoil, and c is the airfoil chord) and the sudden turbulent breakdown at around $s/c = 0.14$, followed by the subsequent formation and convection of an energetic LEV. The LEV and the secondary vortex always spread rearward at 45 % and 30 % of the free-stream velocity, respectively, independent of the reduced frequency. The lift stall occurred when the LEV reached about 90 % of the chord, while the moment stall occurred at the sudden turbulent breakdown. Furthermore, by correlating the MHFS signals with the dynamic-load loops, the variations in the C_l–α curve, especially the stall angle delay and the lift increment prior to, during, and after the stall, were characterized and quantified. It is believed that the various observed unsteady boundary-layer and stall events will also have a direct influence on the flow structure of the tip vortex thus generated. So far, only three experimental investigations (Freymuth, Finaish & Bank 1985; Ramaprian & Zheng 1998; Chang & Park 2000), to the author's knowledge, with a limited frequency and amplitude range, have been reported in the literature.

Ramaparian & Zheng (1998) studied the near field of the tip vortex behind a square-tipped oscillating NACA 0015 rectangular wing by using a three-component laser Doppler anemometer at $Re = 1.8 \times 10^5$ with $\alpha(t) = 10^\circ + 5^\circ \sin \omega t$ (i.e. the light-stall oscillation case) and κ $(= \pi f c/u_\infty$, where f is the oscillation frequency and t is the time$) = 0.1$. They explored the unsteady velocity and vorticity fields associated with the evolving tip vortex in the near field for $x/c = 0.16$–2.66, and observed that the trajectory of the oscillating tip vortex was nearly the same as for a stationary wing at the mean incidence. The normalized circulation distribution across most of the inner part of the vortex for $x/c > 0.7$ exhibited the same universal behaviour as the vortex behind a stationary wing. More recently, Chang & Park (2000) examined the hysteretic behaviour of the wake behind a NACA 0012 airfoil oscillated with $\alpha(t) = 15^\circ + 15^\circ \sin \omega t$ (i.e. the deep-stall oscillation case) at $\kappa = 0.09$ for $Re = 3.4 \times 10^4$ by using a triple-hot-film probe at $x/c = 0.5$ and 1.5. Chang & Park found that the size of the vortex core was larger, and the peak tangential velocity and the axial velocity deficit were smaller, during pitch-down than during pitch-up. Also, because of the massive LEV-induced flow separation, the circulation or vortex strength of the tip vortex at a given α was greater during pitch-up than during pitch-down. However, no detailed vortex flow field information was reported in their Technical Note.

In summary, it is now well known that wing oscillations lead to various complex unsteady flow phenomena accompanied by large variations in the dynamic airloads; however, much work is still needed to better understand and control the tip vortex

generated behind an oscillating wing under the influence of different oscillation frequencies and amplitudes. The objective of this study was to investigate the downstream development of the three-dimensional flow structure of a tip vortex in the near field ($x/c = 0.5$–3.0) behind a sinusoidally oscillated NACA 0015 wing with $\kappa = 0.09$–0.18 at $Re = 1.86 \times 10^5$ by using a triple-hot-wire probe. Oscillation conditions corresponding to attached-flow, light-stall, and deep-stall cases (or oscillations within, through, and well beyond the static-stall angle) were tested. Special attention was given to the spatial–temporal behaviour of the phase-locked ensemble-averaged crossflow and axial velocity fields, the turbulence structure, and the strength, size and trajectory under the influence of different oscillation amplitudes and frequencies. A static-wing tip vortex was also examined to serve as a comparison. Lift-induced drag coefficients were also computed and compared with the force-balance data. It is anticipated that these extensive measurements, covering a complete range of wing oscillations, will deepen our knowledge and understanding of the tip vortices generated by an oscillating wing and their control.

2. Experimental apparatus and methods

The experiments were carried out in the $0.9 \times 1.2 \times 2.7$ m suction-type subsonic wind tunnel at McGill University with a free-stream turbulence intensity of 0.05 % at 35 m s^{-1}. A square-tipped, rectangular NACA 0015 wing with a chord of 20.3 cm, a semi-span b of 50.8 cm and an AR of 2.5 was used to generate the tip vortex (figure 1a). The wing model was mounted horizontally at the centre of the sidewall of the wind tunnel test section. A $0.48 \times 60 \times 60$ cm aluminium endplate with sharp leading edges was fixed to an end support, located 10 cm from the sidewall of the test section. The gap between the wing and the endplate was kept at less than 1 mm to minimize the leakage of flow through the gap. The origin of the coordinate system was located at the trailing edge of the wing-tip with the x-, y-, and z-axes in the streamwise, normal, and spanwise directions, respectively. A servomotor was used to provide the sinusoidal motions at various oscillation amplitudes and frequencies of the wing about its quarter-chord. The mean incidence α_m of the oscillation was set at 8°, 14°, and 18°, respectively, with the amplitude $\Delta\alpha$ fixed at 6°, which allowed the wing to be oscillated within, through, and well beyond (corresponding to the attached-flow, light-stall, and deep-stall oscillation cases, respectively) the static-stall angle $\alpha_{ss} = 15°$. The reduced frequency was set at $\kappa = 0.09$, 0.12, and 0.18. The oscillation frequency was measured to an accuracy of ± 0.02 Hz. Information on the phase angle and instantaneous direction of the wing motion (i.e. pitch-up or pitch-down) during the oscillation cycle was obtained from both the servomotor feedback resolver and a potentiometer mounted on the servomotor shaft. Figure 1(b) shows the typical sinusoidal outputs compared with a mathematically generated sine wave form. Also, in the following discussion, the suffix u is used to indicate pitch-up when α is increasing and d is used to indicate pitch-down when α is decreasing.

The instantaneous velocities were subsequently ensemble averaged over 40–80 oscillating cycles to obtain phased-locked averages of the flow properties at various phase positions during the cycle. A miniature triple-hot-wire probe (Auspex Model AVEP-3-102 with a measurement volume of 0.5 mm^3) was used to measure the mean and fluctuating velocity components. The mean flow fields behind the static wing were also examined by using a seven-hole pressure probe (with an outside diameter of 2.4 mm). The pressure probe and triple-hot-wire probe were calibrated *in situ*, following the calibration procedures described by Wenger & Devenport (1999) and

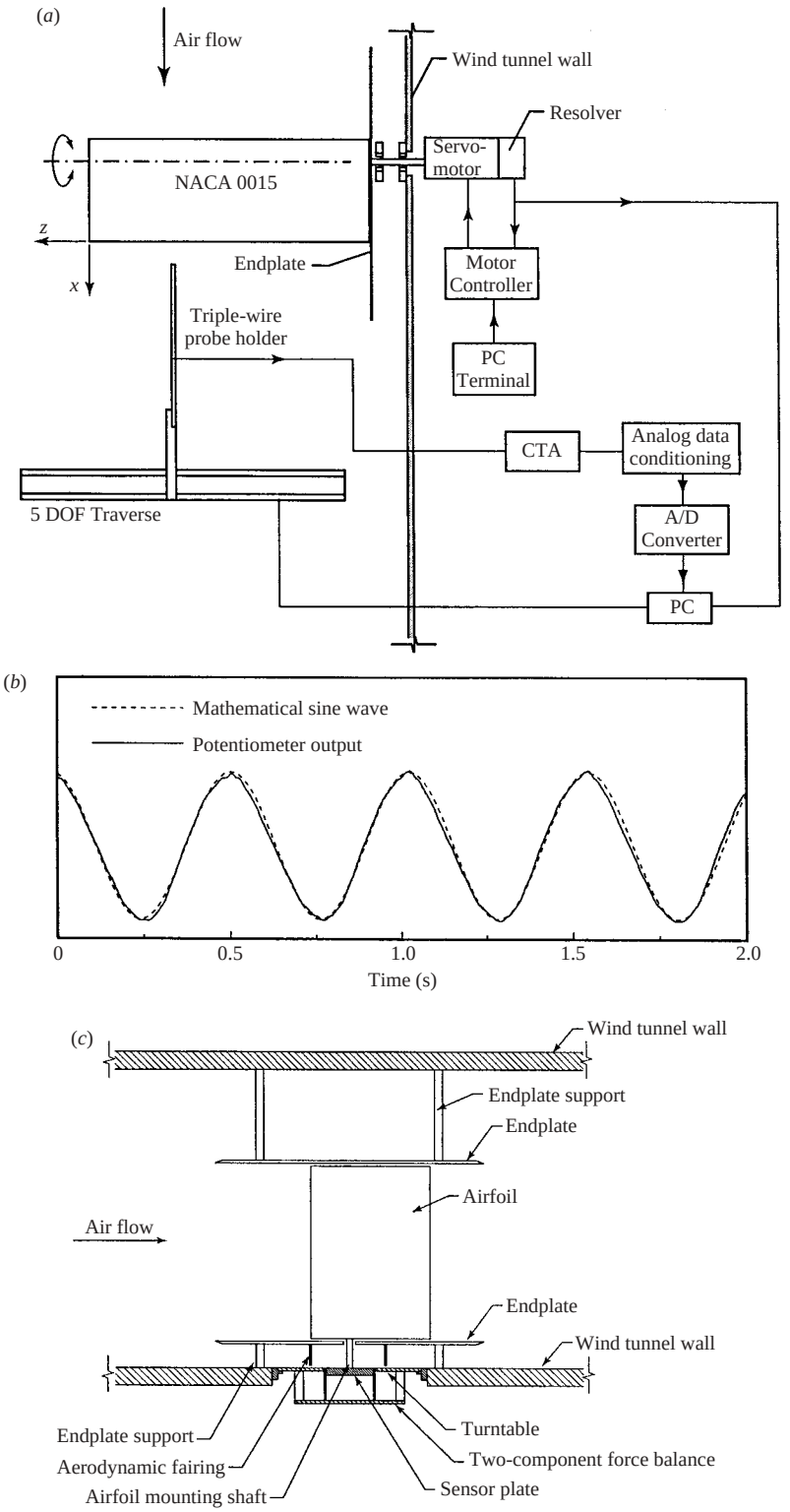

FIGURE 1. Schematics of (*a*) oscillating-wing experimental setup and (*c*) static-wing force-balance system. (*b*) Typical wave form outputs.

Chow *et al.* (1997), respectively, before the installation of the model. The pressure and hot-wire signals were sampled at 500 Hz and were recorded on a PC through a 16-bit A/D converter board. Probe traversing was achieved through a custom-built computer-controlled traversing system with a position resolution in all three directions of 20 μm. The three-dimensional velocities downstream of the trailing edge of the wing were measured in planes perpendicular to the free-stream velocity at six downstream locations: $x/c = 0.5$, 1.0, 1.5, 2.0, 2.5, and 3.0. Data planes taken in the near field of the wing models had 46×46 measuring grid points with an increment of $\Delta y = \Delta z = 3.2$ mm. A finer $\Delta y = \Delta z = 1.6$ mm was also employed to document the core-flow characteristics. The free-stream velocity was fixed at 14.4 m s^{-1}, which rendered a chord Reynolds number of 1.86×10^5.

The maximum experimental uncertainties in the results reported have been estimated as follows (Birch & Lee 2004): mean velocity 3.5 %, vorticity component 8 %, vortex radius 4 %, and velocity fluctuation 3 %. No wind-tunnel wall corrections were made to the present measurements. Furthermore, it is known that the lateral excursions to which a trailing vortex is prone when situated in a free stream containing ambient turbulence has long caused problems in measurement of vortex characteristics, and that the meander amplitude is linearly proportional to the level of free-stream turbulence and to the downstream distance from the generating lifting surface. In the present low-turbulence wind tunnel, the meander amplitude was very small because of the low level of turbulence. However, the vortex meandering in the near field behind the generating wing was examined by using the correlation technique/criteria employed by Chow *et al.* (1997). The meandering of the vortex was determined to be small and did not contribute appreciably to the present measurements.

For static-wing lift and drag force measurements, the models were mounted vertically on an external two-component force balance located below the wind tunnel (figure 1*c*). The airfoil model was mounted vertically between two $0.45 \times 60 \times 60$ cm aluminium endplates with sharp leading edges. The bottom plate was fixed to the bottom wall of the test section and an aerodynamic fairing was placed around the shaft to isolate it from the tunnel flow. The top endplate was mounted on the top wall of the test section. The gaps between the airfoil and the endplates were kept at less than 1 mm to minimize leakage of flow through the gaps. Details of the force-balance system are given in Birch & Lee (2004). This two-dimensional configuration with no free end effects will hereafter be referred to as the two-dimensional wing configuration with $C_{L,2-d}$ and $C_{D,2-d}$ denoting the corresponding total lift and drag coefficients, respectively. Furthermore, by removing the top endplate, the total lift coefficient, $C_{L,3-d}$, and drag coefficient, $C_{D,3-d}$ ($= C_{Dp} + C_{Di}$, where C_{Dp} is the profile drag coefficient and C_{Di} is the lift-induced drag coefficient) of a three-dimensional wing configuration were also obtained. Estimated uncertainties of C_L and C_D measurements were 4 % and 7 %, respectively.

3. Results and discussion

3.1. *Static wing*

To facilitate the investigation of the effects of wing oscillations on the near-field vortex flow structure, the tip vortex generated by a static NACA 0015 wing positioned at $\alpha = 2°$–$19°$ for $Re = 1.86 \times 10^5$ was characterized first and served as a frame of reference for the oscillating wing results. Particular attention was given to the variation of the critical vortex flow quantities and C_{Di} with x/c and α.

3.1.1. *Variation of vortex flow with x/c*

Figures 2(*a*)–2(*g*) depict the typical evolution of the vortex, in terms of the mean streamwise vorticity $\zeta c/u_\infty$ contours, both along the tip ($x/c = -0.5$, -0.25 and -0.1) and in the near wake ($x/c = 0.05$, 0.5, 1.0 and 1.5) of a static wing at $\alpha = 10^\circ$. The dashed line denotes the position of the wing trailing edge. The presence of the multiple secondary vortices around the tip at $x/c = -0.5$ (figure 2*a*), and its wrapping around the main vortex as it progressed down the chord can be clearly seen from the streamwise vorticity contours. As x/c increased (figures 2*b* and 2*c*), the region of high vorticity increased (in both area and magnitude) as the main vortex gained strength from the feeding sheet of boundary-layer vorticity, and these secondary structures were eventually entrained by the main vortex. Immediately downstream of the trailing edge of the wing ($x/c = 0.05$; figure 2*d*), the vorticity from the shear layers leaving the trailing edge was rigorously carried into the vortex. The iso-vorticity contours, however, show very asymmetric or developing patterns at this measuring station. Further downstream, the tangential velocity v_θ and vorticity distributions were attaining axisymmetry and the axial velocity deficit was reducing (as illustrated in figure 3). At $x/c = 0.5$ (figure 2*e*), a tip vortex with nearly axisymmetric tangential velocity profiles (i.e. $v_{\theta max} \approx v_{\theta min}$) and ζ distributions already existed in the inner region of the vortex. The flow outside the core was dominated by the remainder of the wing wake which wound into an ever-increasing spiral (see also figure 2*j*). The degree of axisymmetry became more pronounced with the downstream distance (figures 2*f*–2*g*).

Figures 2(*h*)–2(*j*) illustrate the typical mean cross-flow velocity vectors and the axial mean u/u_∞ and fluctuating u'/u_∞ velocity contours at $x/c = 1.0$. It can be seen that at $x/c = 1.0$, the flow consisted of a small concentrated vortex core (of radius $0.06c$) surrounded by a circulating velocity (figure 2*h*). The vortex centre was taken as the location of maximum vorticity. The axial flow was, however, observed to form islands of velocity which both exceeded and fell behind the free-stream value (figure 2*i*), a phenomenon which persisted up to $x/c = 2.0$ in the present experiment. The observed islands of wake- and jet-like axial velocity distributions could be attributed to the following two controlling mechanisms (Shekarriz *et al.* 1993): (i) the momentum deficit caused by the boundary layer on the wing, and (ii) the axial variation of the core tangential velocity which gives rise to a change in the axial velocity. The radial diffusion of the tangential momentum generally results in an increase in the core pressure and a reduction in the axial velocity, a phenomenon typically observed within a decaying or expanding vortex. On the other hand, during vortex roll-up, v_θ increases with x/c, creating a negative axial pressure gradient ($\mathrm{d}p/\mathrm{d}x < 0$) and, consequently, an increase in the axial velocity. The boundary layer on the wing and vortex roll-up, therefore, have opposite effects. In addition, since $\mathrm{d}p/\mathrm{d}x$ also depends on the radial position, it is often observed that in some portion of a tip vortex there is axial momentum deficit, whereas in another a momentum excess.

Figures 3(*a*)–3(*d*) show the distributions of the non-dimensional v_θ, ζ, u and u' through the vortex for $x/c = 0.05$—2.0 at $\alpha = 10^\circ$. All profiles are measured parallel to the y-axis. As expected, v_θ changed sign from negative to positive on crossing the vortex core from pressure to suction (figure 3*a*). Outside the core-flow region v_θ varied inversely with the radius (r^{-1}) and asymptotically approached a value of zero; a behaviour typical of a tip vortex. For $x/c < 0.5$ (i.e. before the attaining of vortex axisymmetry), v_θ was higher on the suction side by as much as 9 %, i.e. with $v_{\theta max} - v_{\theta min} = 0.09u_\infty$. This discrepancy decreased rapidly with increasing x/c. For

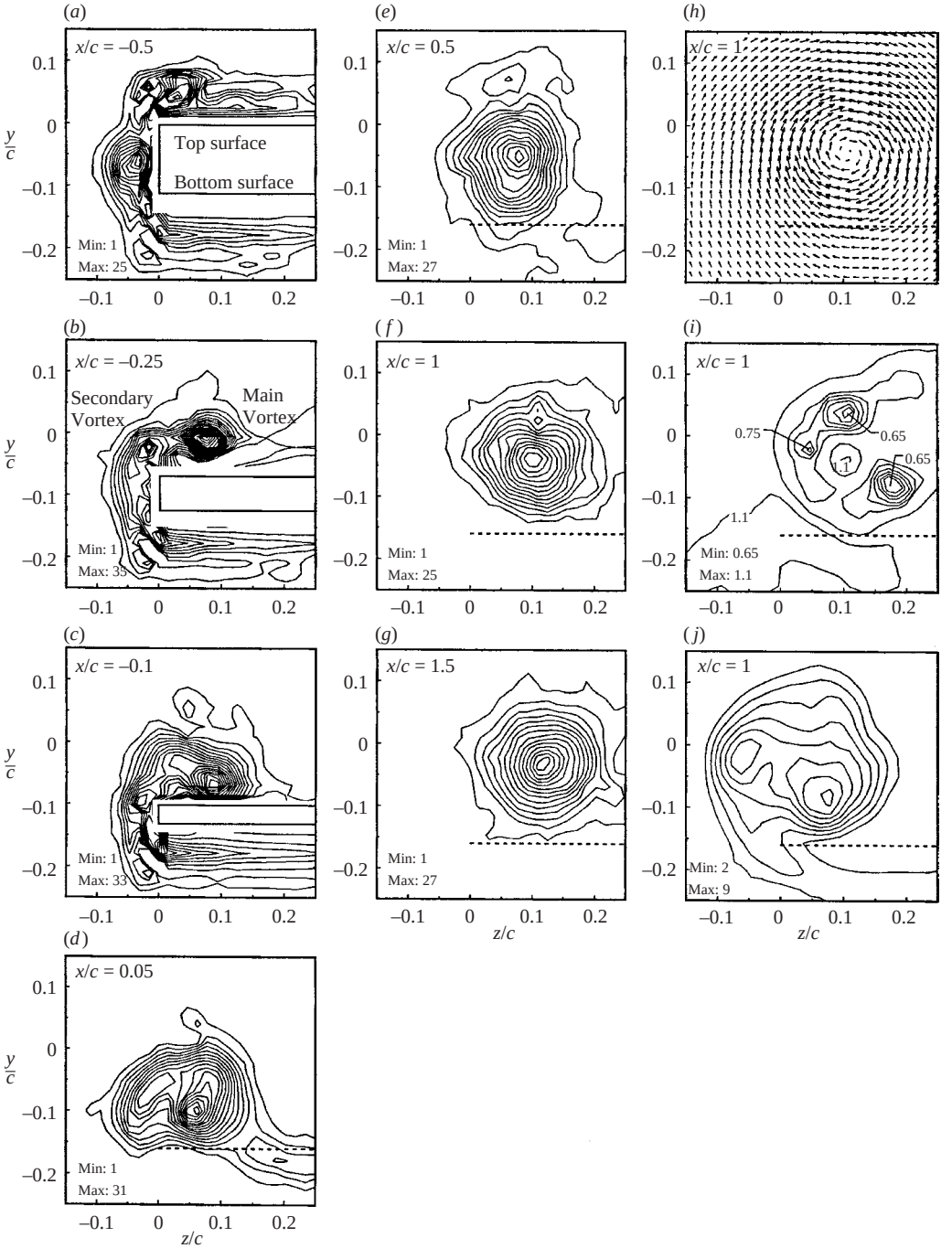

FIGURE 2. Typical normalized static-wing vortex flow structures at $\alpha = 10°$: (*a–g*) streamwise mean vorticity contours $\zeta c/u_\infty$ for $x/c = -0.5$ to 1.5. For $x/c = 1.0$: (*h*) mean vw-velocity vectors, and axial (*i*) mean u/u_∞ and (*j*) fluctuating u'/u_∞ velocity. Numerical values denote $\zeta c/u_\infty$, u/u_∞, and u'/u_∞ (%) levels with constant increments of 2, 1, and 4, respectively.

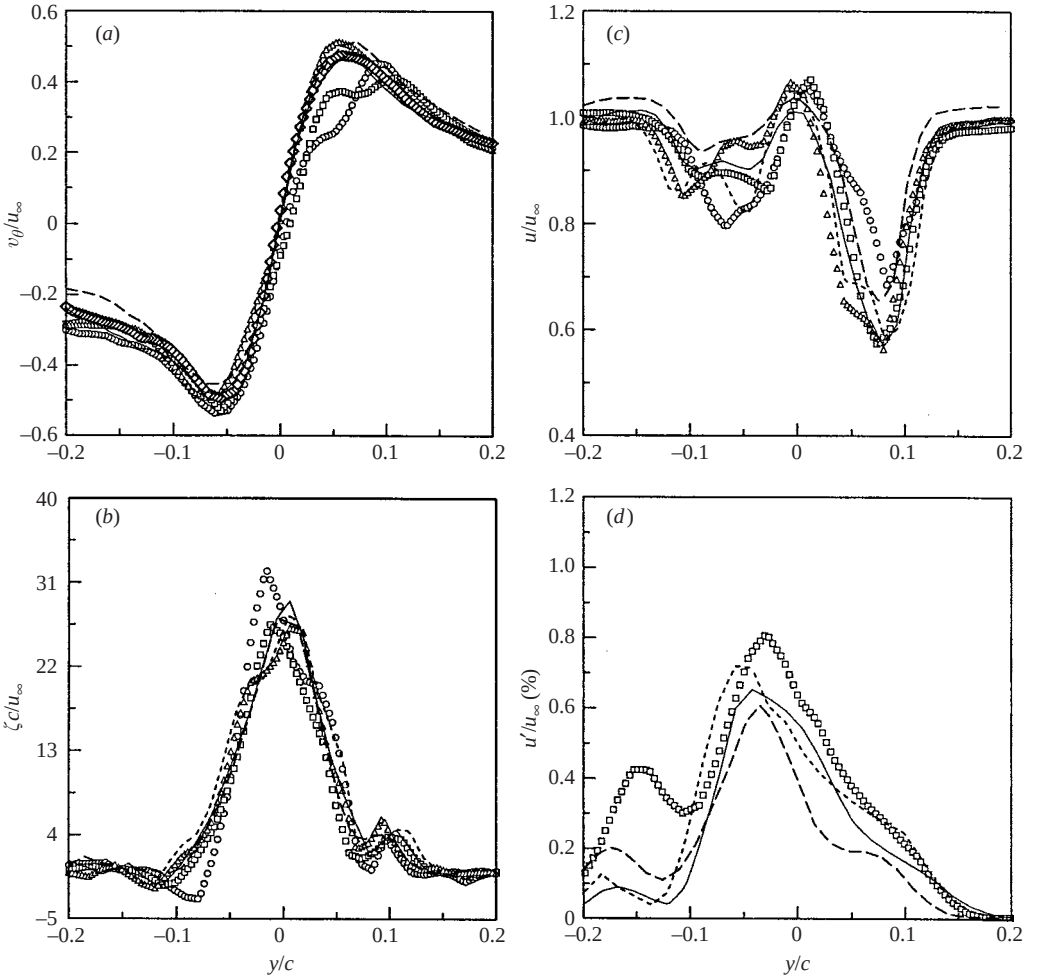

FIGURE 3. Typical normalized static-wing vortex flow distributions across the vortex centre at $\alpha = 10°$. (*a*) v_θ/u_∞, (*b*) $\zeta c/u_\infty$, (*c*) u/u_∞, and (*d*) u'/u_∞ (%). ○, $x/c = 0.05$; □, $x/c = 0.15$; Δ, $x/c = 0.3$; ·····, $x/c = 1.05$; ——, $x/c = 1.5$; ----, $x/c = 2$.

$x/c = 0.5$–2.0, the tip vortex clearly attained axisymmetry with $v_{\theta max} = v_{\theta min}$ within measurement error and was accompanied by a constant circulation. For all the x/c investigated, the vorticity was highest at the centre of the vortex and approached zero outside of the core (figure 3*b*). The u/u_∞ profiles shown in figure 3(*c*) not only reflect the islands of wake- and jet-like distributions shown previously in figure 2(*j*), but also indicate that about $0.1c$ outboard of the core, the structure of the flow appeared much like that of a two-dimensional turbulent wake behind a circular cylinder with a minimum u of about $0.6u_\infty$; a small jet-like core axial velocity u_c of $1.03u_\infty$ (associated with a peak u'; figure 3*d*) in the vicinity of the vortex core was also observed.

Figure 4 summarizes the variation of the non-dimensional critical vortex flow quantities and C_{Di} with x/c at $\alpha = 10°$. The peak tangential velocity $v_{\theta peak}$ and vorticity ζ_{peak} decayed slightly for $x/c = 0.3$ to 2.0 (figure 4*a*). The core axial velocity u_c was of small jet-like flow in the near field. The core radius r_c (defined as the radius at which v_θ is a maximum) was found to increase slightly with x/c while the outer

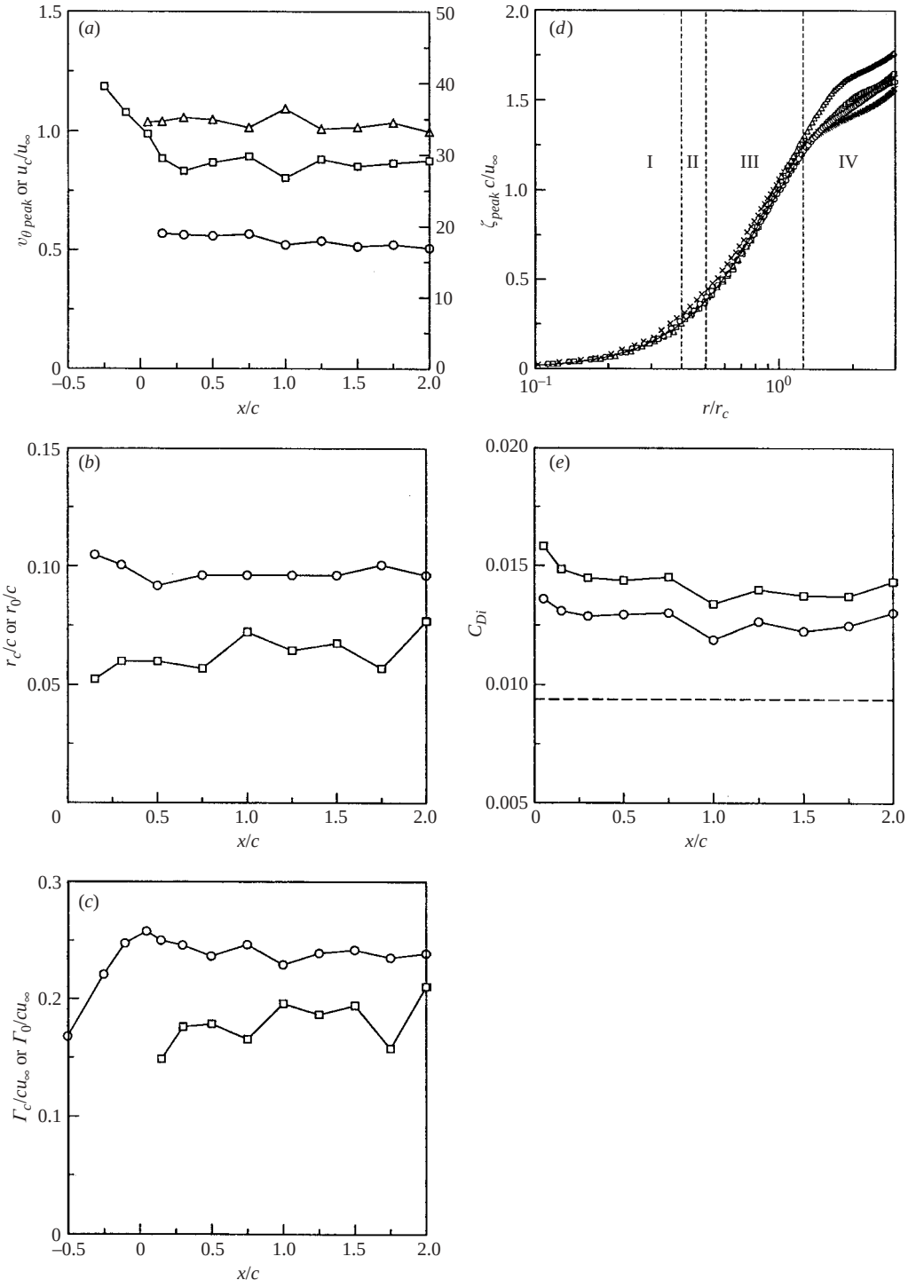

FIGURE 4. Variation of (*a*) ○, $v_{\theta peak}/u_\infty$; □, $\zeta_{peak}c/u_\infty$; Δ, u_c/u_∞; (*b*) □, r_c/c; ○, r_o/c; (*c*) □, Γ_c/cu_∞; ○, Γ_o/cu_∞; (*d*) Γ/Γ_c; and (*e*) C_{Di} (○, equation (4); □, equation (5); ----, $C_{Di} = C_L^2/\pi eAR \times 10^{-1}$) with x/c at $\alpha = 10°$. In (*d*): ○, $x/c = 0.5$; □, $x/c = 1.0$; Δ, $x/c = 1.5$; ×, $x/c = 2$; ·····, equation (3); ----, equations (1) and (2). I: inner-core region, II: buffer region, III: logarithmic region, and IV: outer region.

radius r_o (obtained by measuring the extent as the circulation $\Gamma(r_o)$ reached 98 % of the total circulation Γ_o) remained basically unchanged for $0.3 < x/c < 2.0$ (figure 4*b*). In short, the near-field critical vortex flow quantities, once attaining axisymmetry, did not change significantly with x/c (up to $x/c = 2$ studied); an average $v_{\theta peak} = 0.55u_\infty$, $\zeta_{peak}c/u_\infty = 28$, $u_c = 1.03u_\infty$, $r_c = 0.063c$, and $r_o = 0.098c$ was obtained. Note that according to Moore & Saffman (1973), r_c/c is equal to $2.92(x/c)^{1/2}\mathrm{Re}^{-1/2}$ (= 0.0048–0.107 for $x/c = 0.5$–2.5) for an elliptically loaded wing. In the present experiment, the axial change in r_c/c was, however, quite small and was definitely not proportional to $(x/c)^{1/2}$. Moreover, for the x/c range studied, the tip vortex was found to shift within $0.125c$ inboard of the tip edge at a rate that decreased slightly with x/c.

Figure 4(*c*) indicates that at $\alpha = 10°$, the total circulation, or vortex strength, Γ_o increased quite dramatically along the tip of the airfoil, reaching a local maximum at $x/c = 0.05$ (with $\Gamma_{o,peak}/u_\infty c = 0.253$), and remained rather constant ($\approx 95\,\% \Gamma_{o,peak}$) for $x/c = 0.3$–2.0, suggesting that the roll-up of the inner region of the tip vortex was nearly complete a half-chord downstream of the trailing edge. The circulation, or vortex strength, was calculated either by a line integral over the velocity or by the area integral over vorticity. The line integral was evaluated by repeated applications of the trapezoidal rule and was performed on either circular paths or paths of constant vorticity. The area integral was evaluated by summing the vorticity multiplied with the incremental area of the measuring grid. The observed $\Gamma_o = 0.245u_\infty c = 0.75\Gamma_b$ for $0.3 < x/c < 2.0$ also reveals that immediately downstream of the trailing edge about 75 % of the bound circulation Γ_b was entrained into the vortex. The bound circulation was determined from $\Gamma_b = \frac{1}{2}(K_1 C_L + K_2)u_\infty c$. The constants K_1 and K_2 were determined following the method of Glauert (1926) and C_L is the lift coefficient. Note that the convective velocities of the vortex sheet, when estimated from $u_{conv} = \Gamma/2S$ (S is the wing area; Moore 1974), suggest that roll-up should continue up to $x/c \approx 3.5$ for $\alpha = 10°$. Figure 4(*c*) also reveals that a core circulation $\Gamma_c/u_\infty c$ (= 0.175) of about 73 % of $\Gamma_o/u_\infty c$ was observed in the near field ($0.5 \leqslant x/c \leqslant 2.0$) behind the generating wing, which is consistent with the theoretical value of $\Gamma_c/\Gamma_o = 0.715$ of Lamb's (1945) solution.

The present static-wing measurements also indicate that for a nearly axisymmetric tip vortex in the near field behind the generating wing, the radial distribution of $\Gamma(r)$, normalized by Γ_c, plotted against $\log(r/r_c)$ also shows some interesting characteristics. Figure 4(*d*) indicates that for $x/c = 0.3$–2.0, the distribution of circulation within the tip-vortex core followed a $\Gamma \propto r^2$ profile for $r/r_c < 0.4$ and varied logarithmically for $0.5 < r/r_c < 1.4$. For $r/r_c > 1.4$, Γ continued to vary with x/c, suggesting that for $r > 1.4r_c$, the roll-up of the vortex was only nearly complete and there was a slow addition of vorticity to the outer layers of the vortex from the shear layer arriving from the inboard regions. The observed self-similar behaviour of the inner region of a nearly axisymmetric tip vortex in the near-wake region is of particular interest, since it generally takes a distance of several tens or even hundreds of wing chords downstream for the vortex to become fully developed and attain the characteristics of asymptotic trailing vortices. The empirical curve-fit relationships that describe the inner-core region and the region where the $\Gamma(r)$ distribution is logarithmic, according to Hoffman & Joubert (1963), and Phillips (1981), are

$$\Gamma(r)/\Gamma_c = A(r/r_c)^2 \qquad \text{for } r/r_c < 0.4, \tag{1}$$

$$\Gamma(r)/\Gamma_c = B\log(r/r_c) + C \quad \text{for } 0.5 < r/r_c < 1.4. \tag{2}$$

The curve-fit constants obtained as a function of x/c are listed in table 1. Furthermore, for $0.3 < x/c < 2$, all the data within $0 < r/r_c < 1.2$ collapsed onto a sixth-order

Static wing:							
α(deg.)	A	B	C	x/c	A	B	C
4	1.727	1.969	0.994	1.30	1.393	2.215	0.946
6	1.574	1.985	0.955	1.50	1.566	2.230	0.994
8	1.666	2.010	0.972	1.75	1.667	2.110	0.974
10	1.566	2.230	0.994	2.00	1.786	1.942	0.962
12	1.619	1.197	0.978	2.25	1.611	2.208	0.997
14	1.811	2.154	0.986	2.50	1.805	1.927	0.965
16	1.586	2.178	0.994	2.75	1.707	2.042	0.969
18	1.609	2.070	0.970	3.00	2.029	1.893	0.994
Oscillating wing ($\alpha(t) = 18^\circ + 6^\circ \sin \omega t$ and $\kappa = 0.09$):							
$x/c = 1$:				$\alpha_u = 18^\circ$:			
α	A	B	C	x/c	A	B	C
$\alpha_u = 13^\circ$	1.727	1.969	0.994	1	1.393	2.215	0.946
$\alpha_u = 18^\circ$	1.574	1.985	0.955	1.5	1.566	2.230	0.994
$\alpha_u = 22^\circ$	1.666	2.010	0.972	2	1.667	2.110	0.974
$\alpha_d = 19^\circ$	1.566	2.230	0.994	2.5	1.786	1.942	0.962
$\alpha_d = 16^\circ$	1.619	1.197	0.978	3	1.611	2.208	0.997
$\alpha_d = 13^\circ$	1.811	2.154	0.986				

TABLE 1. Curve-fit constants of equations (1) and (2) for an oscillating wing.

polynomial (similar to that reported by Ramaprian & Zheng 1997 and Birch & Lee 2004) with an autocorrelation coefficient of 0.998:

$$\Gamma(r)/\Gamma_c = 1.756(r/r_c)^2 - 1.044(r/r_c)^4 + 0.263(r/r_c)^6. \tag{3}$$

Finally, the lift-induced drag coefficient C_{Di} ($= D_i/\frac{1}{2}\rho_\infty u_\infty^2 S$, where D_i is the induced drag force) was also computed based on the vorticity inferred from the measured velocity field by using Maskell's (1973) induced-drag model at different downstream distances (figure 4*e*). The vw-crossflow velocity vectors within the measurement plane were decomposed into a stream function $\psi(y, z)$ and a velocity potential $\phi(y, z)$ with the imposed boundary conditions requiring both ψ and ϕ to be zero on the edges of the measurement plane. The lift-induced drag was then obtained by

$$D_i = \tfrac{1}{2}\rho_\infty \int_{S_\zeta} \int \psi \zeta \, \mathrm{d}y \, \mathrm{d}z - \tfrac{1}{2}\rho_\infty \int_{S1} \int \phi \sigma \, \mathrm{d}y \, \mathrm{d}z \tag{4}$$

where ζ is the vorticity, the surface S_ζ is the region within $S1$ where the vorticity is non-zero, σ $(= \partial v/\partial y + \partial w/\partial z)$ is a source term, and the flow is incompressible. Similar to the trend in Γ, the C_{Di} had a local maximum of 0.0138 at $x/c = 0.05$ and reduced slightly for $0.3 < x/c < 2.0$. Also shown in figure 4(*e*) are the C_{Di} obtained from

$$D_i = \int_{S2} \int \tfrac{1}{2}\rho_\infty (v^2 + w^2) \, \mathrm{d}y \, \mathrm{d}z \tag{5}$$

as suggested by Brune (1994) and Kusunose (1997). It can be seen that for a nearly axisymmetric tip vortex with small streamwise pressure gradients the two results, calculated by equations (4) and (5), agree well with each other; the C_{Di} computed by equation (4), however, had, a slightly higher value. Also shown in figure 4*e* are the C_{Di} values estimated from $C_{Di} = C_L^2/(K + 1/\pi e A R)$ (denoted by the dashed line). K is the pressure-drag magnification factor and has a typical value of 0.007

(Naik & Ostowari 1990), and $e = 0.9$ is the Oswald wing-span efficiency factor. The results show that Prandtl's classical lifting-line theory overpredicts the C_{Di} (an order of magnitude larger) for the present near-field low-Reynolds-number experiment with an $AR < 4$.

3.1.2. *Variation of vortex flow quantities with* α

The variation of the non-dimensional critical vortex flow quantities and C_{Di} with α at $x/c = 1.0$ is presented in figures 5 and 6. Also shown in figures 6(g) and 6(h) are the variation of C_L and C_D with α. Figures 5(a) and 5(b) display the composite plots of the contour maps of $\zeta c/u_\infty$ of a static wing at different α. The nearly axisymmetric distributions of the streamwise mean vorticity for $\alpha = 2°$–$19°$ and the presence of islands of wake- and jet-like axial wakes are exhibited for $\alpha = 12° - 19°$. Note that for $\alpha < 12°$, the axial flow was wake-like. Figure 6(a) shows that, as expected, the increase in C_L or α resulted in a significant linear increase in $v_{\theta peak}$ and ζ_{peak} up to $\alpha \leqslant \alpha_{ss} = 15°$, and was followed by a reduction as $\alpha > \alpha_{ss}$. Also, the vortex-core axial flow switched from being wake-like to jet-like at $\alpha \approx 12°$. A similar trend was also observed in the change of r_o and r_c, Γ_c and Γ_o, and C_{Di} with α (figures 6b–6d). For $\alpha \leqslant \alpha_{ss}$, a basically constant ratio of $r_c/r_o = 0.64$, $\Gamma_c/\Gamma_o = 0.73$ and $\Gamma_o/\Gamma_b = 0.75$ was observed. It is important to note that the lift-induced drag was found to contribute to no more than 20 % of the total drag of the wing model, determined directly with a force balance (figures 6g–6h), for the Reynolds number tested. The self-similar behaviour of the inner flow of the vortex for $\alpha = 2°$–$18°$ following equations (1) and (2) also persisted. The coefficients of equations (1) and (2) as a function of α are listed in table 1. Moreover, a direct comparison of the levels and radial growth of the vortex strength $\Gamma(r)$ plotted against the radius r of the tip vortex at different α is also summarized in figure 6(e). The significant increase in the level of Γ with α was evident. Note that for largely unseparated conditions, i.e. the linear lift range, the vortex did not shift appreciably (figure 6f).

3.2. *Oscillating wing*

The effects of wing oscillations on the vortex flow characteristics and the lift-induced drag for $x/c = 0.5$–2.5 were investigated and compared with their static counterparts. Sinusoidal oscillations both within and beyond α_{ss} were tested with reduced frequency $\kappa = 0.09$, 0.12, and 0.18.

3.2.1. *Wing oscillated within* α_{ss}

For a NACA 0015 wing oscillated with $\alpha(t) = 8° + 6° \sin \omega t$ (i.e. with $\alpha_{max} < \alpha_{ss}$) and $\kappa = 0.18$, the overall vortex structure did not appear to be significantly different from that of a static wing (figures 2a and 5a) at the same α, especially during pitch-up. However, the delay of the flow separation (due to the boundary-layer improvement effects as suggested by Ericsson & Reding 1988) led to a more axisymmetrically distributed inner vortex flow of decreased vortex strength, compared to a baseline wing. The details of the phase-locked ensemble-averaged vw-velocity vectors and the contours of the streamwise vorticity, axial mean and fluctuating velocities at $x/c = 1.0$ were regenerated and are illustrated in figure 7 for $\alpha_u = 10°$ (during pitch-up) and $\alpha_d = 10°$ (during pitch-down). Note that the data are shown only for instantaneous $\alpha(t) = 10°$ at $\kappa = 0.09$ and 0.18 for the sake of clarity.

Figure 7(a) shows that at $x/c = 1.0$, the flow outboard of the wing followed a nearly circumferential path about the vortex centre; however, inboard, there was a strong radial flow away from the vortex centre. The dashed lines denote the instantaneous location of the wing trailing edge. For a NACA 0015 wing oscillated with $\kappa = 0.18$

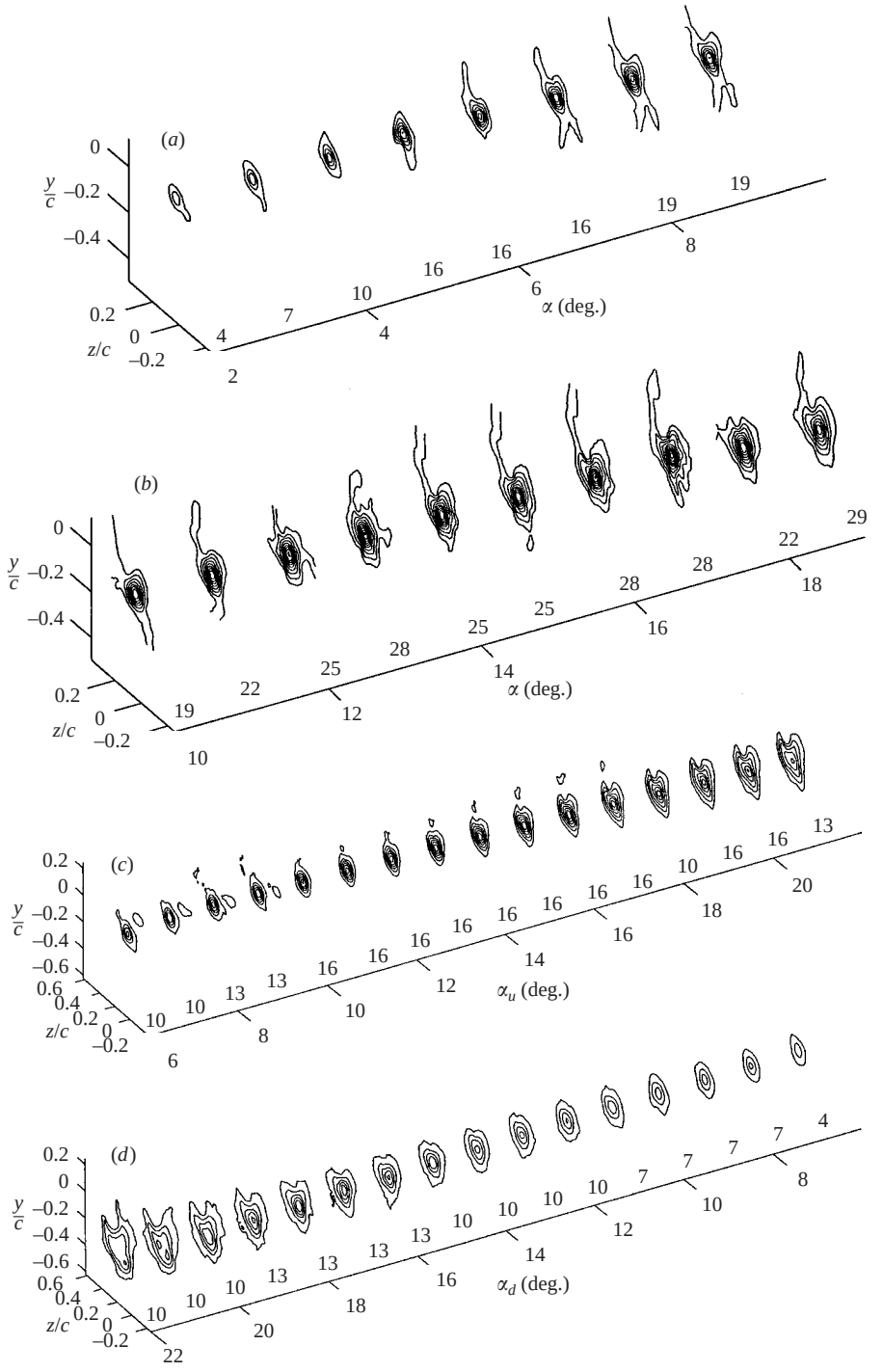

FIGURE 5. Composite plots of normalized mean streamwise vorticity $\zeta c/u_\infty$ at $x/c = 1.0$. (a, b) static wing, and (c, d) $\alpha(t) = 14^\circ + 6^\circ \sin \omega t$ and $\kappa = 0.18$. Numbers inside plots denote maximum $\zeta c/u_\infty$.

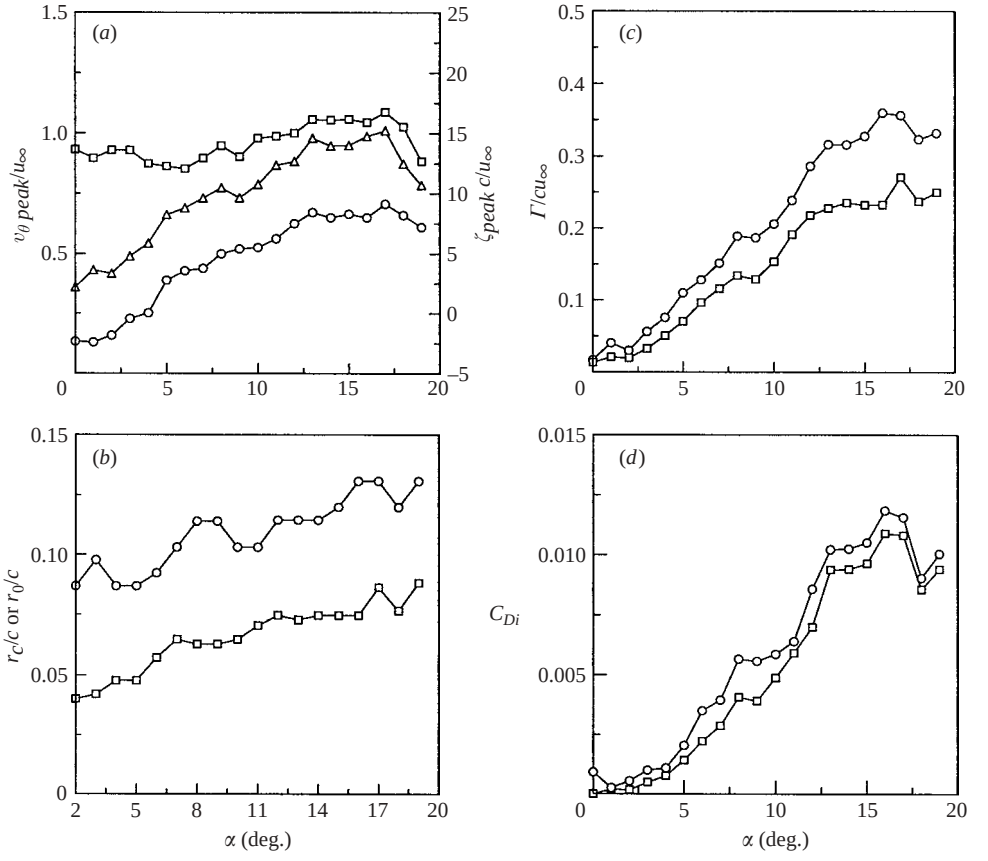

FIGURE 6(*a–d*). For caption see next page.

and $\alpha_{max} = 14°$, the axial flow was observed to be wake-like during pitch-up whereas it had islands of wake- and jet-like flows during pitch-down (figures 7*a*, 7*b* and 7*c*), which is similar to a static wing at the same α. The vorticity distributions were more organized and less diffusive, compared to their static counterparts, and had higher levels during pitch-down than during pitch-up. Note that the spiral (corresponding to the shear layer from the inboard regions of the flow, which was in the process of rolling up to form the axial tip vortex) was generally slightly more organized during pitch-up motion than during the pitch-down motion at lower κ ($=0.09$). The vortex was more tightly wound with a lower vorticity level and a weaker axial flow distribution (figures 7*c* and 7*d*).

Figures 8(*a*)–8(*f*) display the distributions of v_θ/u_∞, $\zeta c/u_\infty$, u/u_∞, u'/u_∞, and $\Gamma/u_\infty c$ across the tip vortex at $x/c = 1.0$ and $\alpha_u = \alpha_d = 10°$ for $\kappa = 0.09$–0.18. Also shown in figure 8 are the results for a static wing at the same airfoil incidence. The axisymmetric behaviour of v_θ and ζ (figures 8*a* and 8*b*) in the inner region of the vortex and their decay to nearly zero in the outer part of the vortex, which are qualitatively similar to those observed in a classical steady viscous trailing vortex in the near field behind a static wing, is apparent. Both ζ and v_θ across the inner region of the vortex varied considerably during the oscillation cycle and were smaller than those of a static wing. The tip vortex was, however, of lower (higher) core vorticity (tangential velocity) during pitch-up (pitch-down), and with values decreasing with κ

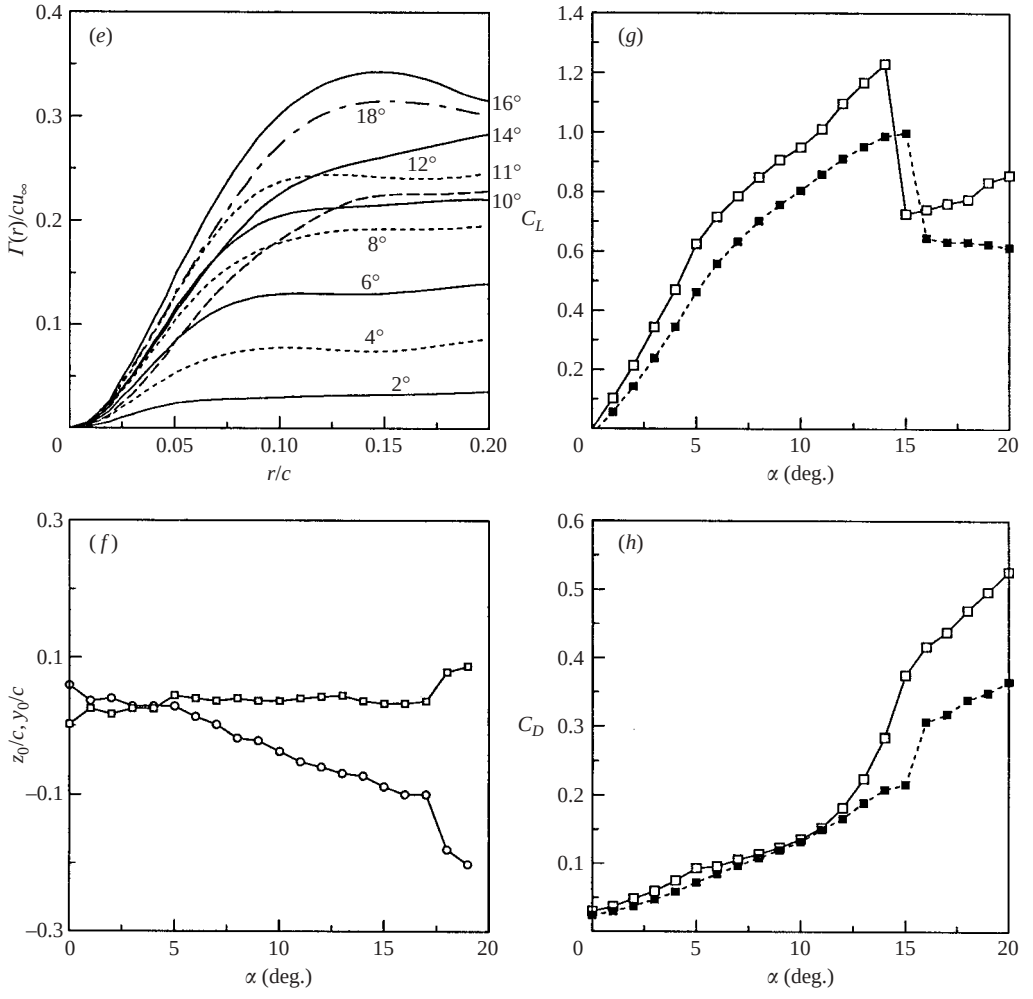

FIGURE 6. Variation of (*a*) ○, $v_{\theta peak}/u_\infty$; Δ, $\zeta_{peak}c/u_\infty$; □, u_c/u_∞; (*b*) □, r_c/c; ○, r_o/c, (*c*) □, Γ_c/cu_∞; ○, Γ_o/cu_∞, (*d*) C_{Di} (□, equation (4); ○, equation (5)); (*e*) $\Gamma(r)$, and (*f*) vortex trajectory (□, z_o/c; ○, y_o/c) with α at $x/c = 1.0$. (*g*) C_L (□ $C_{L,2-d}$; ■, $C_{L,3-d}$); (*h*) C_D (□, $C_{D,2-d}$; ■, $C_{D,3-d}$).

but increasing with α. It is important to note that for a NACA 0015 airfoil oscillated sinusoidally within α_{ss}, the mean axial velocity was always wake-like during pitch-up while exhibiting islands of wake- and jet-like flows (with a small jet-like core flow; figure 8*c*). The magnitudes of the velocity deficit during pitch-up and the jet-like core flow during pitch-down were found to increase with κ. The variation of u' distributions (figure 8*d*), however, was observed to follow the similar trend of that of a static wing but they were less turbulent. The axial core velocity fluctuations were found to be lower during pitch-up than during pitch-down and were significantly lower than the static-wing values. The core u' increased with κ especially during pitch-up.

Figure 8(*e*) shows that the observed gradual and monotonic increase in circulation with radial distance in the inner region of the vortex behind an oscillating wing is very similar to the behaviour for a static vortex and was clearly indicative of the viscous/turbulent nature of the vortex. The circulation distribution, however, varied

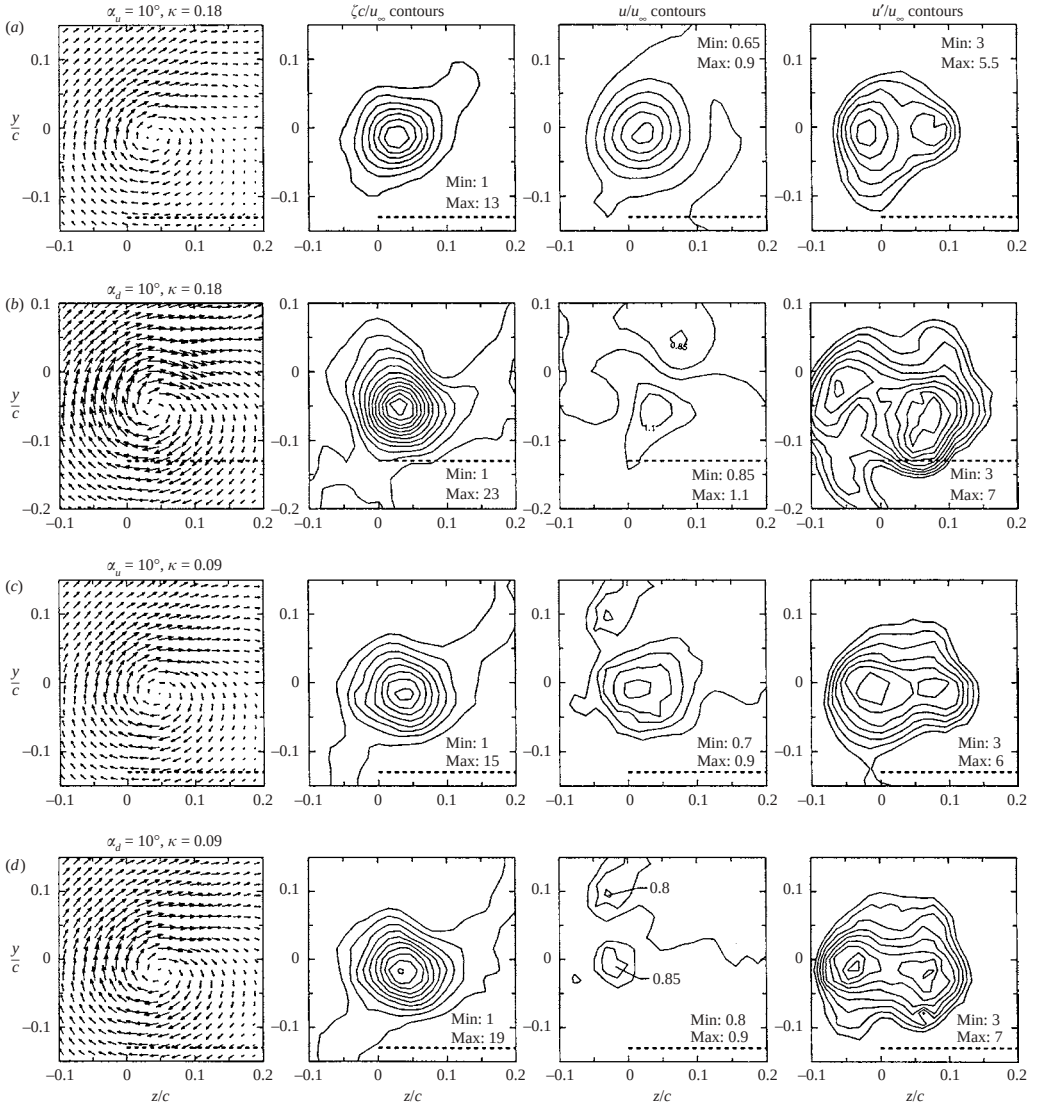

FIGURE 7. Typical phase-locked ensemble-averaged vortex flow structures at $\alpha_u = \alpha_d = 10°$ and $x/c = 1.0$ for $\alpha(t) = 8° + 6° \sin \omega t$. (*a*, *b*) $\kappa = 0.18$; (*c*, *d*) $\kappa = 0.09$. Numerical values denote $\zeta c/u_\infty$, u/u_∞, and u'/u_∞ levels with constant increments of 2, 1, and 4 %, respectively.

considerably during the oscillation cycle and the individual distributions for a given incidence during pitch-up and pitch-down motion did not correspond with each other. Figure 8(*e*) also indicates that the total circulation Γ_o values also show a small but consistent variation with α, due to the continued roll-up of the shear layer and the additional axial vorticity going into the vortex. It is also noteworthy that for a NACA 0015 wing oscillated within α_{ss}, the Γ/Γ_c distributions also exhibited self-similarity in the inner region for $0 < r/r_c < 1.4$ with $x/c > 0.5$ (figure 8*f*), which coincided with the self-similar behaviour observed in the tip vortex behind a static wing. The curve-fit constants of equations (1) and (2) were found to be insensitive to κ, α and x/c.

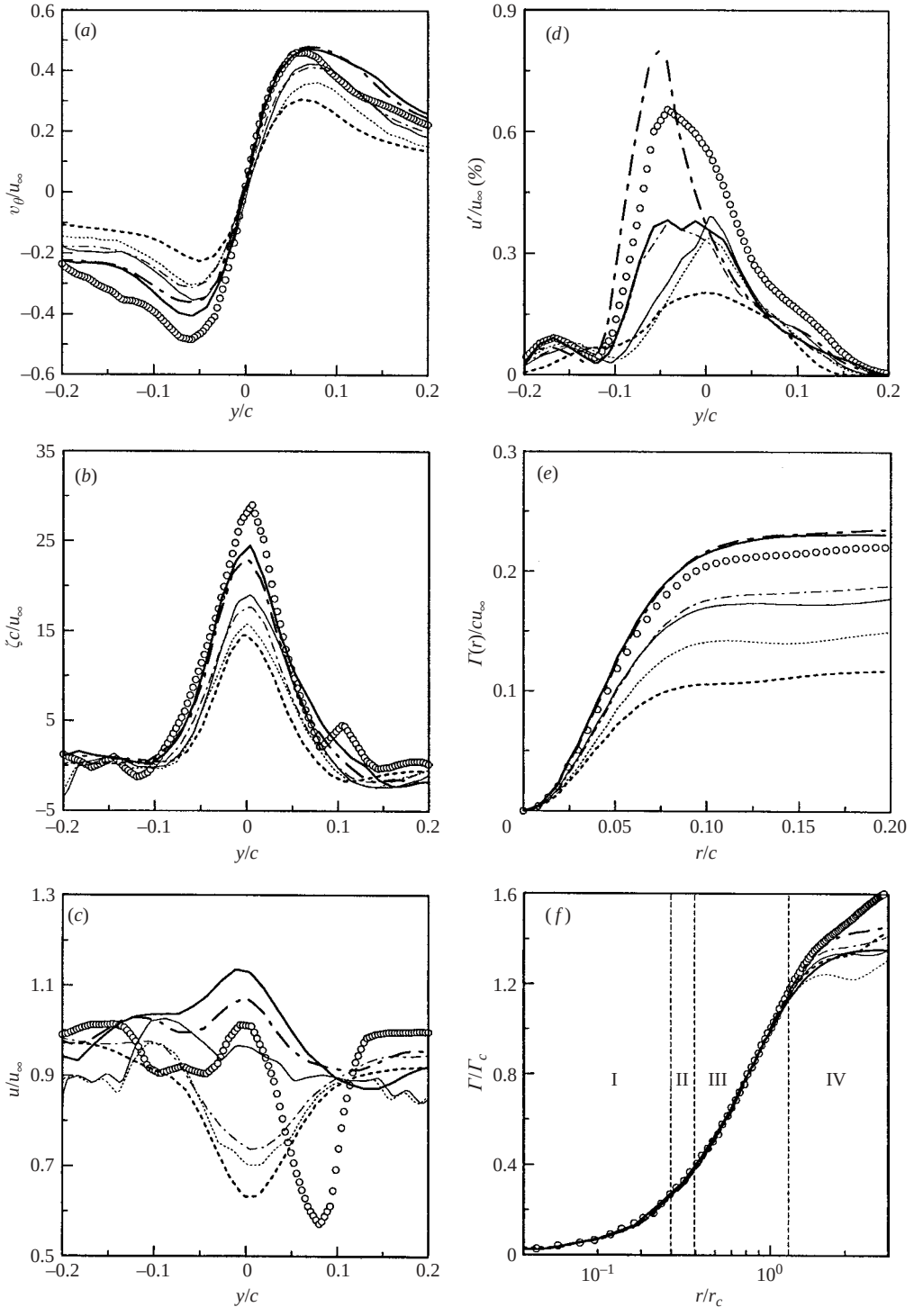

FIGURE 8. Typical distributions of phase-locked ensemble-averaged vortex flow quantities across the vortex at $x/c = 1.0$ for $\alpha(t) = 8° + 6° \sin \omega t$. (*a*) v_θ/u_∞, (*b*) $\zeta c/u_\infty$, (*c*) u/u_∞, (*d*) u'/u_∞ (%), (*e*) $\Gamma(r)/u_\infty c$, and (*f*) Γ/Γ_c. $\kappa = 0.09$: ·····, $\alpha_u = 10°$; ·····, $\alpha_d = 10°$. $\kappa = 0.12$: -·-·-, $\alpha_u = 10°$; -·-·-, $\alpha_d = 10°$. $\kappa = 0.18$: ——, $\alpha_u = 10°$; ——, $\alpha_d = 10°$. ○, static wing.

Pitch-up		Pitch-down	
Uncompensated	Compensated	Uncompensated	Compensated
12	12.00	24	24.13
13	12.74	23	23.38
14	13.51	22	22.61
15	14.30	21	21.79
16	15.13	20	20.93
17	16.02	19	20.01
18	16.97	18	19.03
19	17.99	17	17.98
20	19.07	16	16.87
21	20.21	15	15.70
22	21.40	14	14.50
23	22.62	13	13.26
24	23.87	12	12.00

TABLE 2. Uncompensated and compensated α for $\alpha(t) = 18^\circ + 6^\circ \sin \omega t$ and $\kappa = 0.09$ at $x/c = 1.0$.

Figures 9(*a*)–9(*f*) summarize the dynamic loops of the critical vortex flow quantities and C_{Di} at $x/c = 1$ for $\kappa = 0.09$ and 0.18 during one oscillation cycle. Note that because of the convection time required for a tip-vortex flow structure to propagate from the wing to the downstream location of the sensor, there is a phase lag between any instantaneous sensor reading and the position of the wing at that instant. It is therefore necessary to discuss briefly the phase-lag compensation employed in the present study before the discussion of the dynamic loops displayed in figure 9. Figure 10 shows both the uncompensated and compensated dynamic-circulation loops for $\alpha(t) = 8^\circ + 6^\circ \sin \omega t$ and $\kappa = 0.09$ at $x/c = 1.0$. By assuming that, within the streamwise length scale considered, any streamwise distortion of the flow structure that occurs is negligible, and the convection speed u_{conv} is constant, then the angle of attack through which the wing has swept during the convection time can be directly calculated if u_{conv} can then be approximated. An upper and lower bound is subsequently imposed upon the convection speed, since it cannot fall outside of the range of axial velocities measured within the volume through which it has moved. In the present experiment, u_{conv} was approximated as the upper-bound free-stream speed, since it resulted in the smallest phase lag correction and, by extension, a more conservative result. The phase-lag compensation scheme suggested by Chang & Park (2000), in which u_{conv} was approximated with a spatial average axial velocity in the vicinity of the vortex centre, was also included in figure 10. Note that since some of the measured axial velocities appeared to exceed the free-stream limit, Chang & Park's compensation scheme could somewhat inflate the convection speed. The measurements reported in this study were phase-lag compensated by letting $u_{conv} = u_\infty$. Typical uncompensated and compensated angles of attack at $x/c = 1.0$ for a deep-stall oscillation are listed in table 2.

Figures 9(*a*) and 9(*b*) indicate that similar to the results shown previously in figures 8(*a*) and 8(*b*), the values of $v_{\theta peak}$ and ζ_{peak} were consistently lower than the static-wing values (due to the κ-induced boundary-layer improvement effects), and were higher during pitch-down than during pitch-up. The degree of hysteresis, or asymmetry, increased slightly with κ. The core axial velocity u_c, however, was found to be higher (lower) than the static-wing values during pitch-down (pitch-up),

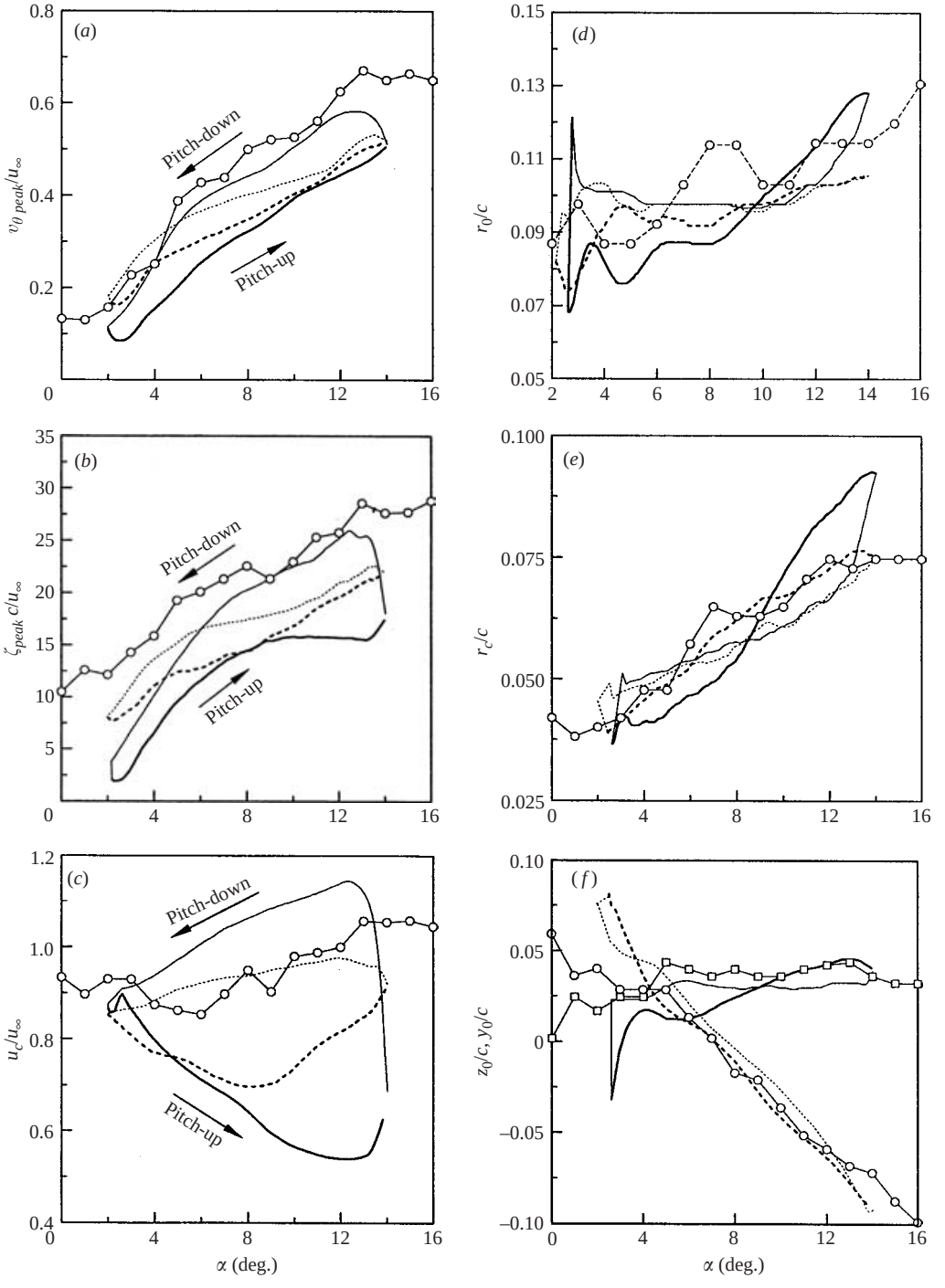

FIGURE 9(*a–f*). For caption see facing page.

especially for $\kappa = 0.18$. Note that for $\kappa = 0.18$, the core vorticity, axial velocity and $v_{\theta peak}$ reached the highest value at $\alpha_u = 13^\circ$ during pitch-up. The maximum tangential velocity and vorticity were decreasing downstream while the change in vortex size

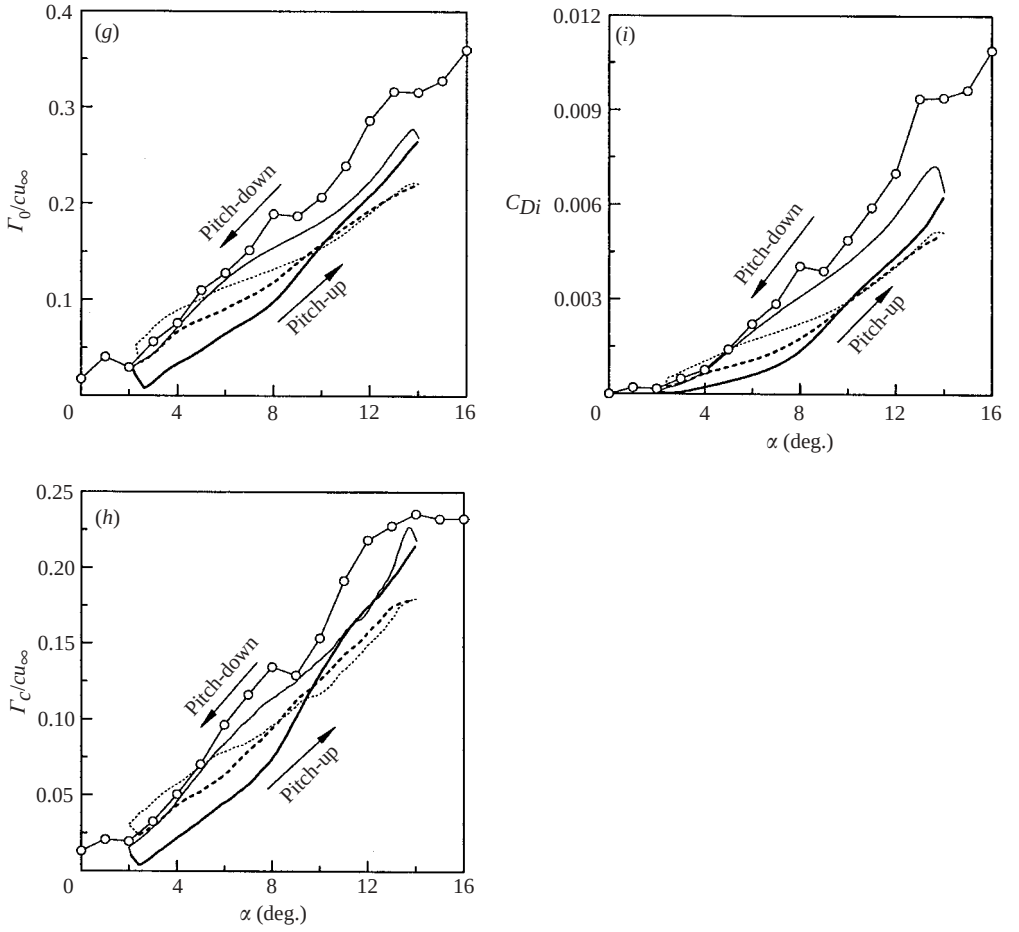

FIGURE 9. Dynamic loops of the critical vortex flow qualities and C_{Di} at $x/c = 1.0$ for $\alpha(t) = 8° + 6° \sin \omega t$ with $\kappa = 0.09$ and 0.18. (*a*) $v_{\theta peak}/u_\infty$, (*b*) $\zeta_{peak}c/u_\infty$, (*c*) u_c/u_∞, (*d*) r_o/c, (*e*) r_c/c, (*f*) vortex trajectory ($\kappa = 0.18$: ·····, y_o/c; ——, z_o/c. static wing: □, z_o/c; ○, y_o/c), (*g*) Γ_o/cu_∞, (*h*) Γ_c/cu_∞, and (*i*) C_{Di}. ·····, $\kappa = 0.09$ and ——, $\kappa = 0.18$. ○, static wing. Thick line: pitch-up; thin line: pitch-down.

was moderate and was insensitive to κ (figures 9*d* and 9*e*). The vortex centre moved with α; it moved slightly inboard from the wing tip and upward (downward) relative to the trailing edge as α increased (decreased) over the oscillation cycle (figure 9*f*).

Figures 9(*g*)–9(*i*) present the dynamic loops of Γ_o, Γ_c and C_{Di} over one oscillation cycle, which clearly demonstrate the small hysteretic property existing between the pitch-up and pitch-down motion. At a fixed x/c, the level of hysteresis in the circulation loops increased slightly with the reduced frequency (figures 9*g*–9*h*). The degree of asymmetry or hysteresis was, however, found to be a weaker function of the downstream distance. The variation of Γ in the near field for $\kappa = 0.09$–0.18 was seen to follow a similar trend to a static wing. The observed lower Γ values during pitch-up than during pitch-down could be attributed to the delay of the transition of the boundary layer, and its subsequent separation from the wing upper surface for a symmetric wing oscillated within α_{ss} (Lee & Gerontakos 2004). Lee & Gerontakos reported that during pitch-up the boundary-layer transition was

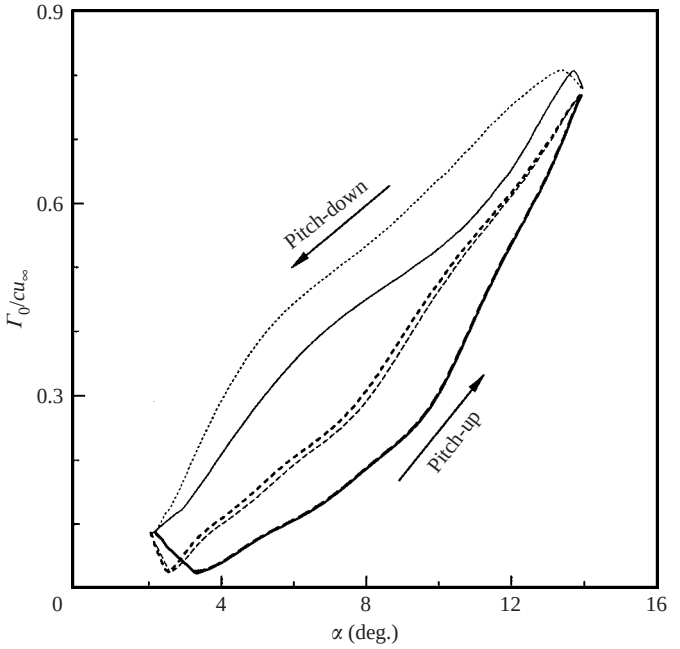

FIGURE 10. Phase-lag compensation for $\alpha(t) = 8° + 6° \sin \omega t$ and $\kappa = 0.18$ at $x/c = 1.0$. ----, uncompensated; ——, present method; · · · · · ·, Chang & Park (2000). Thick line: pitch-up; thin line: pitch-down.

delayed, compared to a static wing, and tended to remain laminar over the majority of the wing surface, rendering a relatively small portion of the boundary-layer flow in the trailing-edge region turbulent, and subsequently resulted in a slightly earlier flow detachment compared to during pitch-down. During pitch-down, the attached turbulent boundary layer extended over a majority of the wing surface, which better withstood the imposed retardation and separation, detached later from the wing surface and resulted in a smaller and less diffusive trailing wake of a higher Γ. Figure 9(*i*) summarizes the variation of C_{Di} (computed by the Maskell method) with κ at $x/c = 1.0$ over an oscillation cycle. The values of C_{Di} were found to increase with α and κ (especially for $\kappa > 0.1$) but varied less noticeably with x/c in the near-wake region. The minima in the C_{Di} loops occurred when the circulation was weakest, or at smallest α. The maxima in the C_{Di} loops occurred when the tip vortex was strongest which, notably, was not at the maximum α (for higher κ values). Similar to the trend observed in Γ, the oscillating wing was found to generate lower lift-induced drag than its static counterparts, and had a higher value during pitch-down than during pitch-up.

3.2.2. *Wing oscillated beyond* α_{ss}

For a NACA 0015 wing oscillated well beyond α_{ss} (i.e. deep-stall oscillation), the behaviour of the tip vortex became more complicated due to the formation, growth and convection of an energetic LEV and its catastrophic detachment from the wing upper surface, in addition to the accompanying large hysteresis in the dynamic-load loops. The deep-stall wing oscillation imposed a strong discrepancy in contour shapes and magnitudes between the pitch-up and pitch-down phases of the oscillation cycle. The iso-$\zeta c/u_\infty$ contours of the tip vortex over an oscillation cycle

for $\alpha(t) = 18^\circ + 6^\circ \sin \omega t$ and $\kappa = 0.09$ at $x/c = 1$ are illustrated in figures 5(*c*)–5(*d*). The qualitative behaviour of the tip vortex, corresponding to the prior to, during, and after stall flow regimes, or conditions, can be explained as follows. The prior-to-stall quasi-steady flow condition consisted of two parts: (i) for $\alpha_u = 12^\circ$ up to about α_{ss} during pitch-up, the boundary-layer flow remained attached, especially over the inboard regions of the wing, which rendered a less turbulent and more organized tip vortex of slightly weaker circulation, compared to their static counterparts, and (ii) for $\alpha_u \approx \alpha_{ss}$ to about 22°, the vortex was observed to be more diffusive and had a higher vortex strength (compared to Part (i)), due to the presence of the turbulent trailing-edge flow reversal and the formation and growth of the LEV on the wing upper surface. During stall (covering $\alpha_u \approx 22^\circ$ to $\alpha_d \approx 20^\circ$), the massive flow separation (over the entire wing upper surface as a result of LEV detachment) leading to the loss of vortex axisymmetry with a sharp decrease (increase) in vortex strength (axial velocity and turbulence levels) can be seen from the ζ, u, and u' iso-contour maps. During the after-stall pitch-down condition (covering $\alpha_d \approx 20^\circ$ to 12°), the tip vortex was of much lower vorticity and the axisymmetry was being re-established (due to the reattachment of the largely separated turbulent flow onto the wing upper surface), compared to the same range of α during pitch-up as well as a static wing at the same incidence.

The axial velocity distributions also indicate that during both pitch-up and pitch-down, the vortex regions always suffered from velocity deficit, in contrast to a static wing at the same α for which the u/u_∞ contours exhibited islands of wake- and jet-like flow distributions. It is shown later in figures 12(*c*) and 13(*c*), that except in the vicinity of α_{max}, the velocity deficit decreased with α, as a result of the largely separated flow from the wing upper surface, during pitch-down rather than during pitch-up. The wake width was found to increase with α. Details of the crossflow vectors and the contours of $\zeta c/u_\infty$, u/u_∞ and u'/u_∞ for $\alpha_u = \alpha_d = 13^\circ$, 18° and 22° at $x/c = 1.0$ were regenerated and are given in figure 11. These specific angles of attack were selected to illustrate the representative tip-vortex flow structures corresponding to the above-mentioned various flow conditions, involving attached flow, flow reversal and LEV growth, LEV detachment, and flow reattachment, as they occur on a wing undergoing deep-stall oscillations. The static-wing results are also included for comparison. The distribution and variation of the phase-locked ensemble-averaged vortex flow quantities across the vortex over an oscillation cycle are presented in figures 12 and 13, respectively.

Figure 11(*a*) shows that at $\alpha_u = 13^\circ$ (i.e. flow regime (i) as described above), as expected, the flow consisted of a small concentrated vortex core (of radius $0.075c$) surrounded by a circulating velocity field that wound the rest of the wing wake into an ever-increasing spiral. The flow outboard of the wing followed a nearly circumferential path about the vortex centre; however, inboard, there was a stronger radial flow away from the vortex centre. The vortex was less tightly wound and had a slightly lower $v_{\theta peak}$ and a much decreased core vorticity, compared to a static wing at $\alpha = 13^\circ$ (figures 12*a*, 12*b*, 13*a* and 13*b*). Both v_θ and ζ across the inner region of the vortex varied considerably during the oscillation cycle and had a significantly higher value during pitch-up than during pitch-down (e.g. compared to $\alpha_d = 13^\circ$ during the pitch-down flow reattachment process). No significant variation in r_c and r_o of the vortex during pitch-up, compared to a static wing, was observed; both r_c and r_o, however, increased drastically above the static-wing values during pitch-down at $\alpha_d = 13^\circ$ (figure 13*c*). Also, the axial velocity at $\alpha_u = 13^\circ$ was wake-like (figure 12*c*), in contrast to a static wing at the same airfoil incidence for which islands of axial

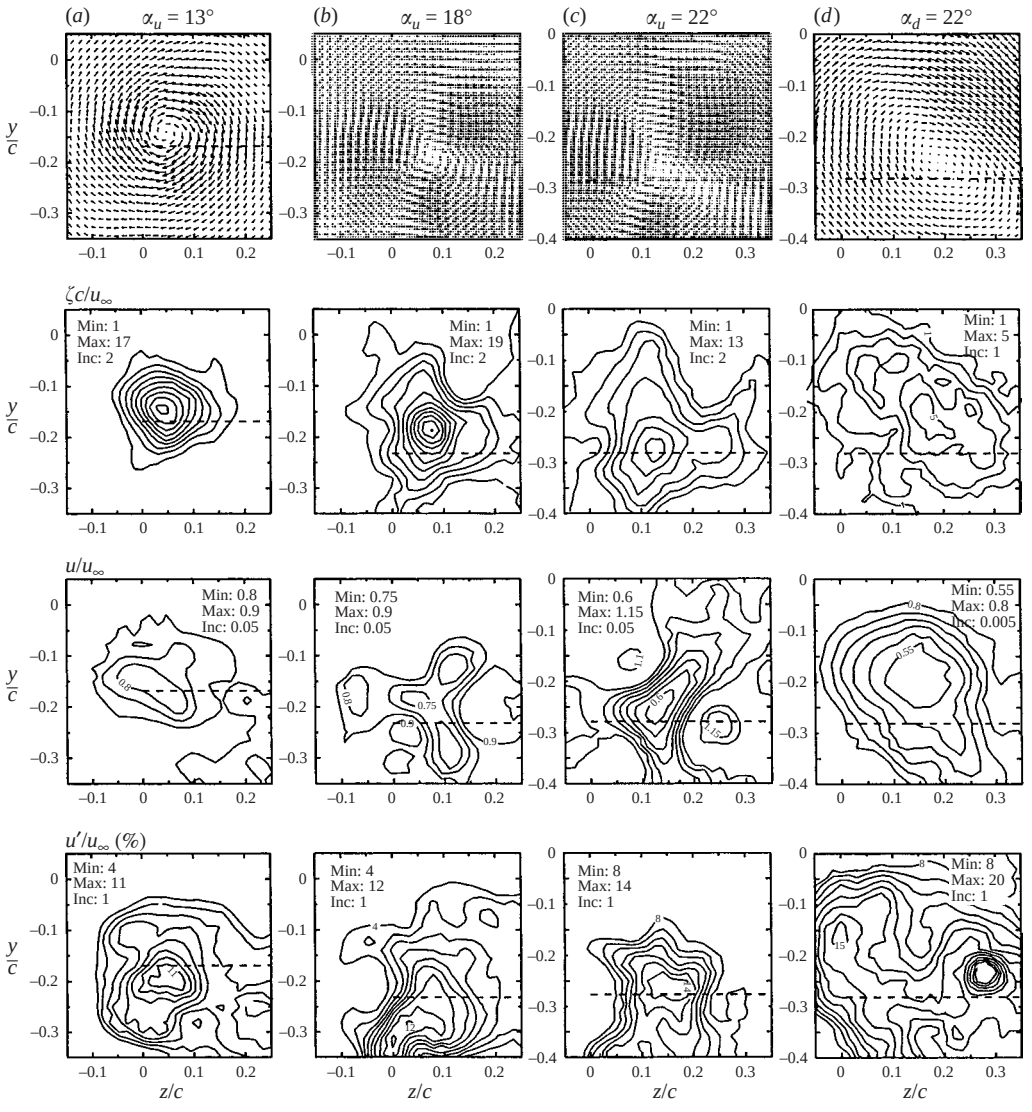

FIGURE 11(*a–d*). For caption see facing page.

velocity both fell behind and exceeded the free-stream value. At $\alpha_u = 13°$, the u' distribution remained similar to that for a stationary wing but with the location of the peak turbulence coinciding with the vortex centre (identified by the location of maximum vorticity). Figure 11(*a*) also indicates that outside the vortex-core region, the axial turbulence structure was clearly dominated by the wake spiral. The spiral (corresponding to the shear layer from the inboard regions of the flow, which was in the process of rolling up to form the axial tip vortex) was generally more organized for the most part during pitch-up than during pitch-down. At $\alpha_d = 13°$ during the pitch-down flow reattachment process (figure 11*f*), the tip vortex was more diffused (of increased r_c and r_o) with a decreased v_θ, rendering a lower vorticity and circulation (due to the agitated flow separation) compared to $\alpha_u = 13°$ during pitch-up as well as

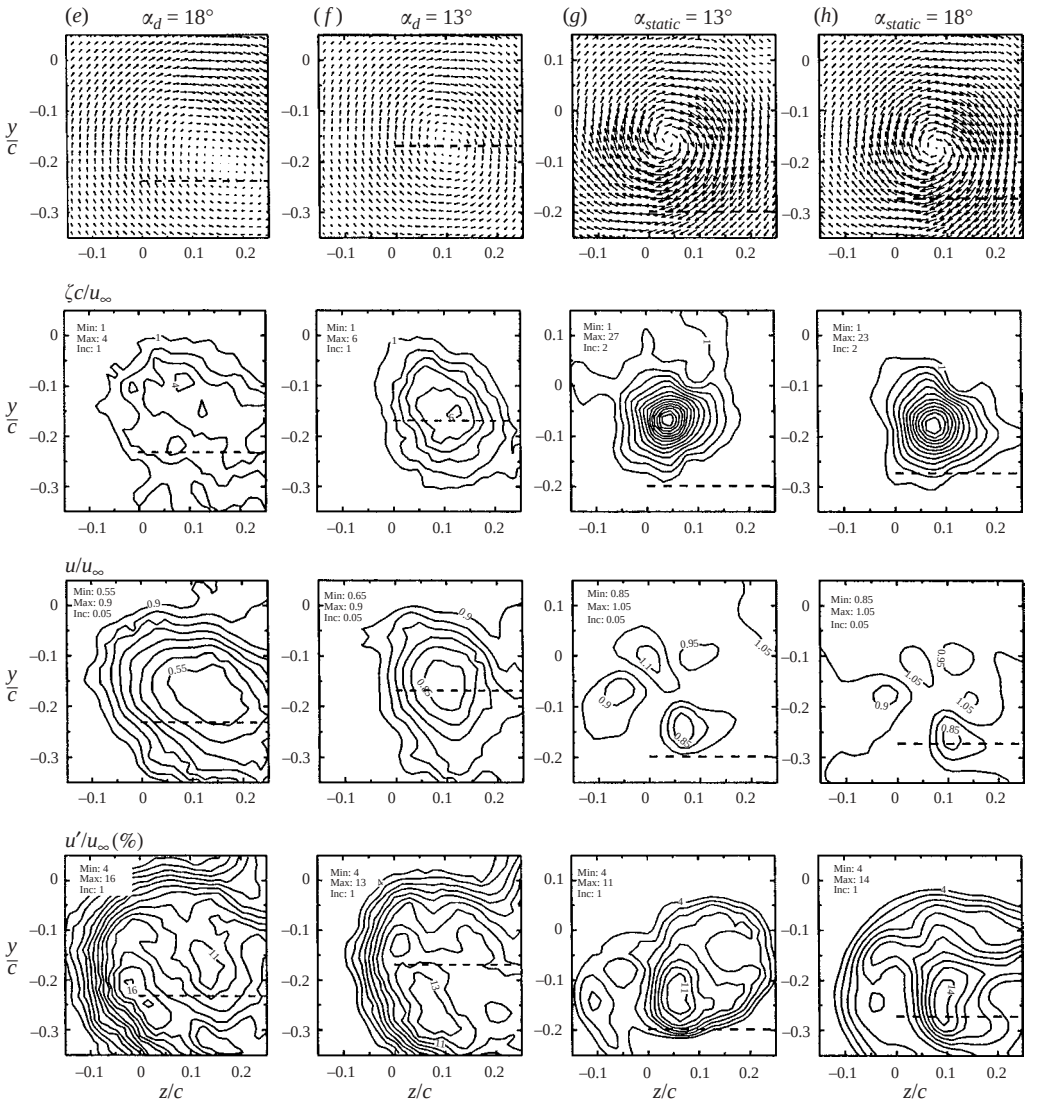

FIGURE 11. Non-dimensional phase-locked ensemble-averaged vortex flow structures at $\alpha_u = \alpha_d = 13°$, 18° and 22° for $\alpha(t) = 18° + 6° \sin \omega t$ and $\kappa = 0.09$ at $x/c = 1.0$. Oscillating wing: (*a*) $\alpha_u = 13°$; (*b*) $\alpha_u = 18°$; (*c*) $\alpha_u = 22°$; (*d*) $\alpha_d = 22°$; (*e*) $\alpha_d = 18°$; and (*f*) $\alpha_d = 13°$. Static wing: (*g*) $\alpha = 13°$ and (*h*) $\alpha = 18°$. Numerical values denote $\zeta c/u_\infty$, u/u_∞, and u'/u_∞ levels with constant increments of 2, 1, and 4, respectively.

a static wing at the same α. A wider and well-defined axial wake profile (resembled that of a circular cylinder) of higher u' was also observed at $\alpha_d = 13°$.

The flow at $\alpha_u = 18°$ ($> \alpha_{ss}$) during pitch-up (i.e. in the aforementioned flow regime (iii)), the vortex remained axisymmetric with less concentrated vorticity distributions (as a result of the significant delay of the flow separation compared to their static counterparts) as can be clearly seen from the crossflow velocity vectors and the vorticity contour maps (figure 11*b*). The magnitude of the cross-stream velocity vectors at $\alpha_u = 18°$ was of the order of u_∞ and was, therefore, quite significant. The tangential velocity variation remained linear in the core regions (figure 12*a*) and was

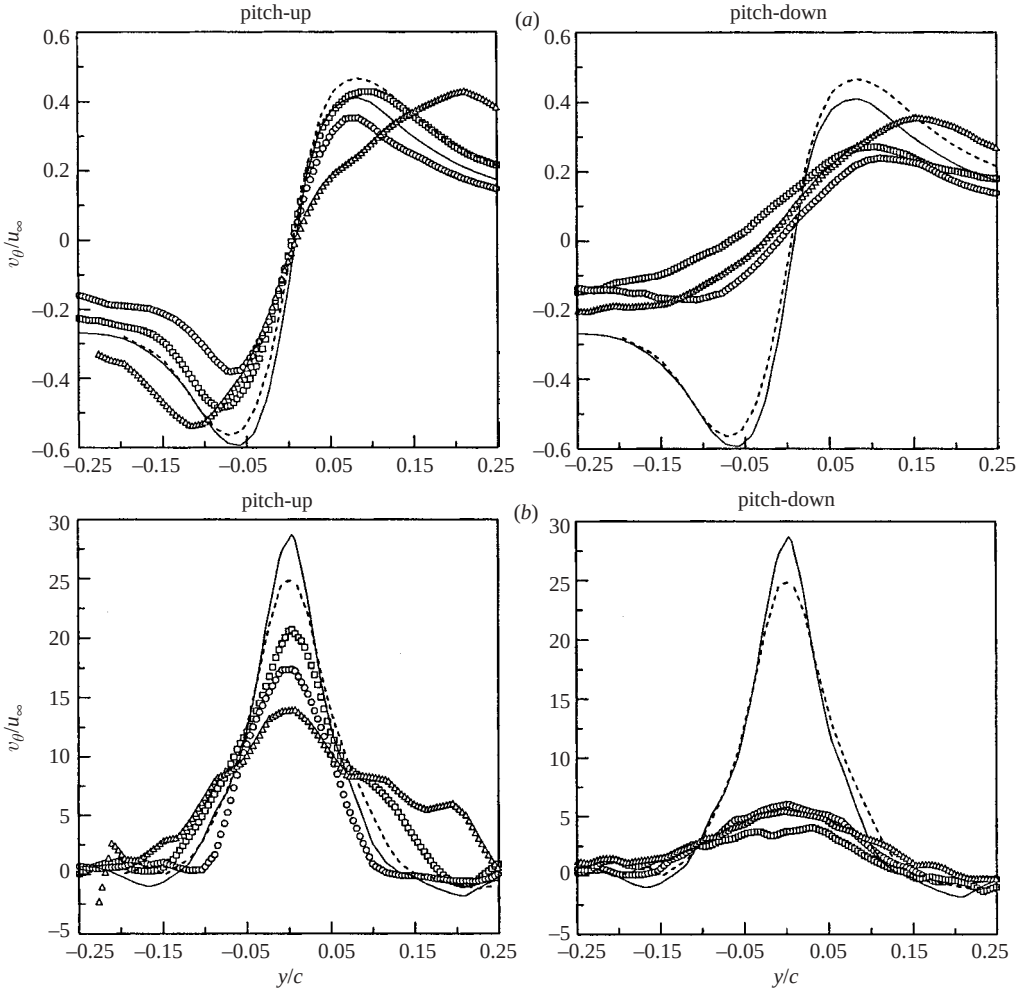

FIGURE 12(*a–d*). For caption see facing page.

much steeper during pitch-up than during pitch-down at $\alpha = 18°$, which resulted in a smaller vortex size (figure 12*c*) and a lower core vorticity distribution during pitch-up (figure 12*b*). During pitch-down at $\alpha_d = 18°$, the peak values of v_θ and ζ (vortex size) were found to be considerably lower (higher) compared to $\alpha_u = 18°$ (figure 11*e*) as well as a static wing at the same α. Note that at $\alpha_d = 18°$ during the pitch-down flow reattachment, the flow was highly agitated, mostly due to the reattaching of the largely separated turbulent boundary layer onto the suction side of the wing, which fed into the vortex and thus resulted in a drastically reduced ζ and v_θ and increased r_c, r_o, u_c and u'.

At $\alpha_u = 22°$ during pitch-up (i.e. immediately before the ultimate growth of the LEV to the full chord length and its subsequent detachment from the wing upper surface), the entrainment of the highly rotational LEV flow into the tip vortex resulted in a more diffused and lowered peak vorticity distribution and an increased r_c and r_o, compared to $\alpha_u = 18°$. An axial flow of both wake- and jet-like velocity profiles, similar to that of a static wing, was observed (denoted by $\triangle$ symbols in figure 12*c*). On the other hand, at $\alpha_d = 22°$ during pitch-down (i.e. in the during-stall flow regime;

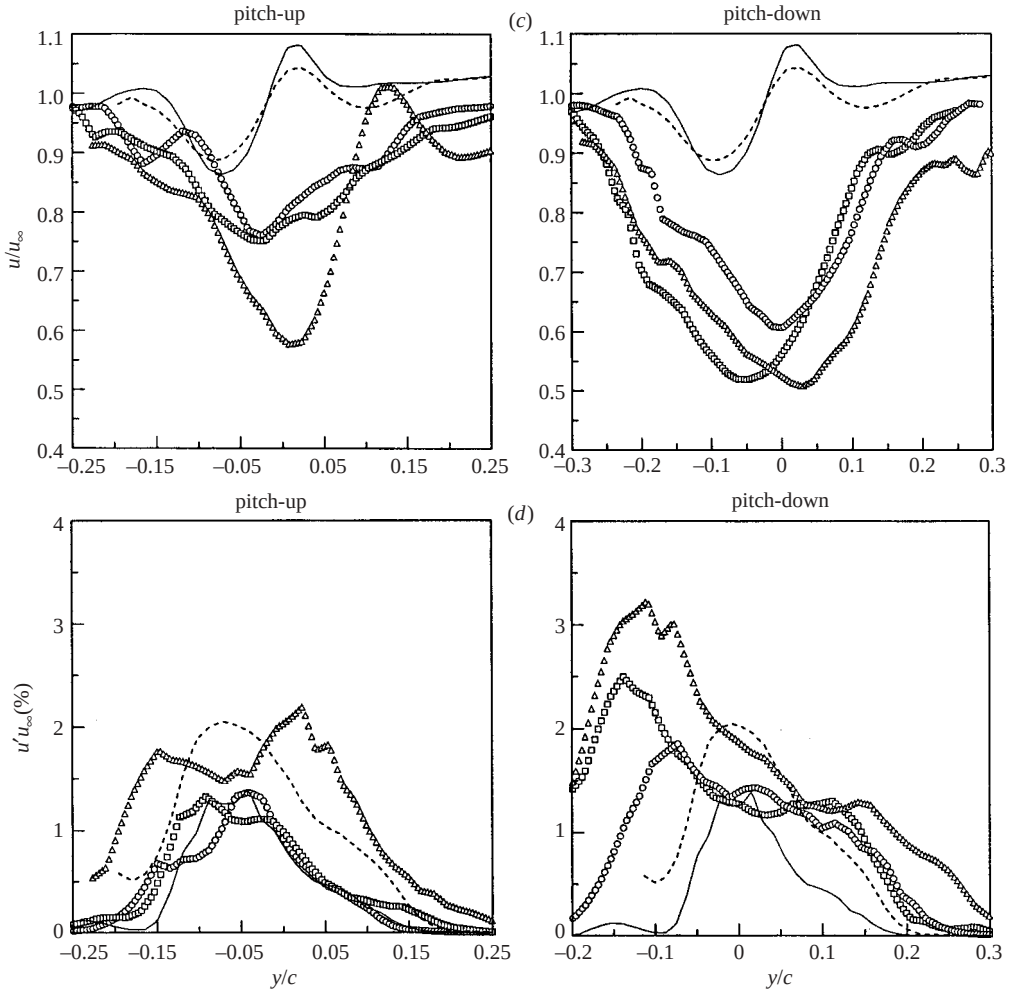

FIGURE 12. Distributions of phase-locked ensemble-averaged vortex flow quantities across the vortex at $\alpha_u = \alpha_d = 13°$, 18° and 22° for $\alpha(t) = 18° + 6° \sin \omega t$ and $\kappa = 0.09$ at $x/c = 1.0$. (*a*) v_θ/u_∞, (*b*) $\zeta c/u_\infty$, (*c*) u/u_∞, and (*d*) u'/u_∞ (%). Oscillating wing: ○, $\alpha = 13°$; □ $\alpha = 18°$; Δ, $\alpha = 22°$. Static wing: ——, $\alpha = 13°$; · · · · · ·, $\alpha = 18°$.

figure 11*d*), the flow separated from the entire wing upper surface, and resulted in an elliptical and highly diffusive tip vortex accompanied by an increased wake width and turbulence level, compared to $\alpha_u = 22°$ during pitch-up. No noticeable difference in the wake velocity deficit was, however, observed between $\alpha_u = 22°$ and $\alpha_d = 22°$.

Figure 13 summarizes the dynamic loops of the non-dimensional $v_{\theta peak}$, ζ_{peak}, u_c, and r_c and r_o, as well as the vortex trajectory at $x/c = 1.0$ and $\kappa = 0.09$ over an oscillation cycle. Figure 13(*a*) indicates that $v_{\theta peak}$ increased with $\alpha(t)$ and was found to be significantly higher during pitch-up than during pitch-down. A local maximum and minimum of 73% of u_∞ and 28% u_∞ at $\alpha_u = 20°$ (corresponding to the sudden breakdown of the turbulent flow in the inboard region of the wing) and $\alpha_d = 13°$ (corresponding to the end of the downstream spread of the reattachment), respectively, were obtained. The rate of change of $v_{\theta peak}$ during both pitch-up and pitch-down, except in the vicinity of α_{max} and α_{min}, was observed to be linear and remained

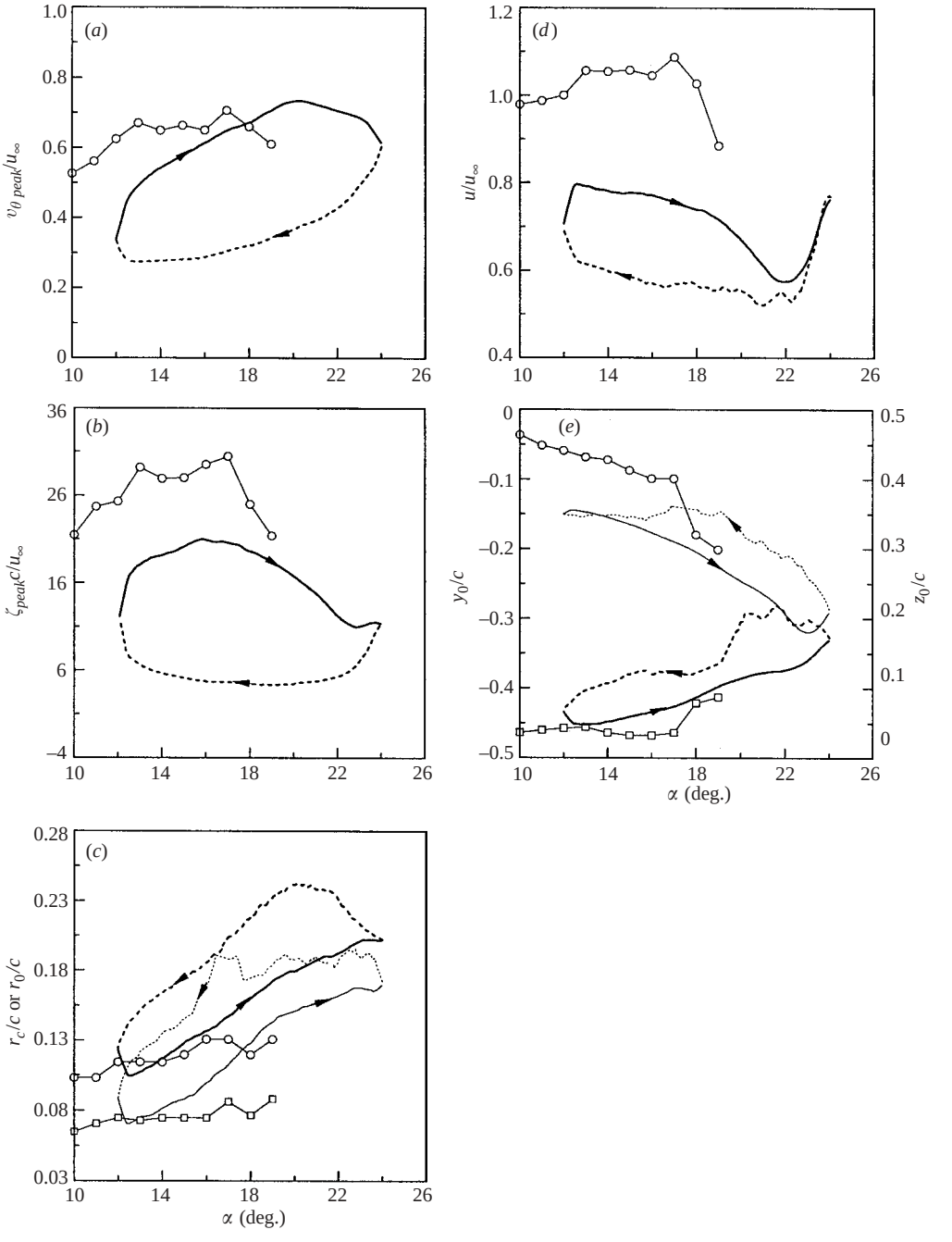

FIGURE 13. Dynamic loops of critical vortex flow quantities over an oscillation cycle for $\alpha(t) = 18° + 6° \sin \omega t$ and $\kappa = 0.09$ at $x/c = 1.0$. (*a*) $v_{\theta peak}/u_\infty$, (*b*) $\zeta_{peak}c/u_\infty$, (*c*) r_c/c and r_o/c (r_c: □, static wing; ——, oscillating wing. r_o: ○, static wing; ——, oscillating wing), (*d*) u_c/u_∞, and (*e*) vortex trajectory (z_o/c: ○, static wing; ——, oscillating wing. y_o/c: □, static wing; ——, oscillating wing). ——, pitch-up; · · · · · ·, pitch-down. ○, static wing.

constant with $\mathrm{d}v_{\theta peak}/\mathrm{d}\alpha$ about 0.033 per degree. Note that due to the asymmetry of the vortex flow at the during-stall flow condition (e.g. in the vicinity of α_{max}), the values of $v_{\theta peak}$ and r_c and r_o were circumferentially averaged and only served as a qualitative reference. The vorticity inside the core reached a maximum value (of $\zeta_{peak}c/u_\infty = 22$) at 16° during pitch-up (corresponding to the onset of the flow reversal), while remaining at a virtually constant value of $\zeta_{peak}c/u_\infty = 5$ during pitch-down flow reattachment from $\alpha_d = 22°$ to 13° (figure 13*b*). Similar to the variation of $v_{\theta peak}$ with $\alpha(t)$, r_c and r_o also exhibited a linear increase (up to the LEV detachment) but had a higher value during pitch-down than during pitch-up (figure 13*c*). A constant growth rate of about $\mathrm{d}(r_o/c)/\mathrm{d}\,\alpha = 0.0129$ and $\mathrm{d}(r_c/c)/\mathrm{d}\,\alpha = 0.0117$ per degree was obtained. The wake-like core axial velocity, or velocity deficit, however, was found to decrease with α and exhibited a much lower value during pitch-down than during pitch-up (figure 13*d*). A local minimum u_c of $0.6u_\infty$ at $\alpha_u = 22°$ during pitch-up (corresponding to the passing of the LEV off the wing trailing edge and the onset of the dynamic stall), followed by a sharp rise and drop in the velocity deficit for $\alpha_u = 22°$ to $\alpha_d = 22°$, was noticed.

Figure 13(*e*) summarizes the movement of the vortex centre relative to the wing tip at the trailing edge during the oscillation cycle (i.e. y_o/c and z_o/c versus α) at $x/c = 1.0$. The vortex centre moved slightly outboard (inboard) from the wing tip and downward (upward) relative to the trailing edge as α increased (decreased) over the oscillation cycle. The vortex centre seemed to extend much farther outboard during pitch-down, implying that much of the circulation (or the spanwise lift distribution) was shed (or shifted) outboard in the sheet and resulted in a weaker circulation (figure 14).

Figure 14(*a*) shows the variation of the circulation $\Gamma(r)/u_\infty c$ with radius r/c at $\alpha_u = 13°$, 18° and 22° and $\alpha_d = 13°$, 16° and 19°. Also shown in this figure are the results for a static wing at $\alpha = 13°$ and 18°. The gradual and monotonic increase in circulation with r of an oscillating wing was similar to a static wing (§ 3.1). Outside the inner-flow region, Γ varied considerably during the oscillation cycle, and the individual distributions for a given α during pitch-up and pitch-down motion did not correspond with each other. Furthermore, by normalizing $\Gamma(r)$ by the core circulation Γ_c and plotting against $\log(r/r_c)$, it is evident that except for the LEV-detachment flow regime (i.e. for $\alpha_u = 22°$ to $\alpha_d = 22°$), the distribution of circulation within the tip vortex core also followed a $\Gamma \propto r^2$ profile for $r/r_c < 0.4$ and varied logarithmically for $0.5 < r/r_c < 1.2$ (figure 14*b*), a phenomenon similar to that of a static wing as well as a wing oscillation with small amplitude. The curve-fit constant of equations (1) and (2) are listed in table 1.

Figures 14(*c*) and 14(*d*) show the dynamic loops of the total $\Gamma_o/u_\infty c$ and core $\Gamma_c/u_\infty c$ circulation over an oscillation cycle at $x/c = 1.0$, which clearly demonstrate the significant hysteretic property existing between pitch-up and pitch-down. Both Γ_c and Γ_o increased with $\alpha(t)$. During pitch-up a significantly higher circulation was observed compared to during pitch-down (due to the massive flow separation, as a result of the LEV detachment and the subsequent flow reattachment process). The Γ values were lower than the stationary-wing values during the pitch-down and during the initial part of the pitch-up. Both Γ_o and Γ_c increased linearly up to $\alpha_u = 21°$ during pitch-up, reached a local maximum (with $\Gamma_o/u_\infty c = 0.51$ and $\Gamma_c/u_\infty c = 0.44$) for $\alpha_u = 21°$ to 23°, and then dropped until $\alpha_d = 18°$. It is significant to note that the rate of increase of Γ_o and Γ_c per unit α during pitch-up, except in the vicinity of α_{max}, was found to be $\mathrm{d}(\Gamma_o/u_\infty c)/\mathrm{d}\,\alpha = \mathrm{d}(\Gamma_c/u_\infty c)/\mathrm{d}\,\alpha = 0.033$ per degree, which is similar to the growth rate of the peak tangential velocity with $\alpha(t)$ (i.e. $\mathrm{d}(v_{\theta peak}/u_\infty)/\mathrm{d}\,\alpha = 0.033$ per degree) during pitch-up.

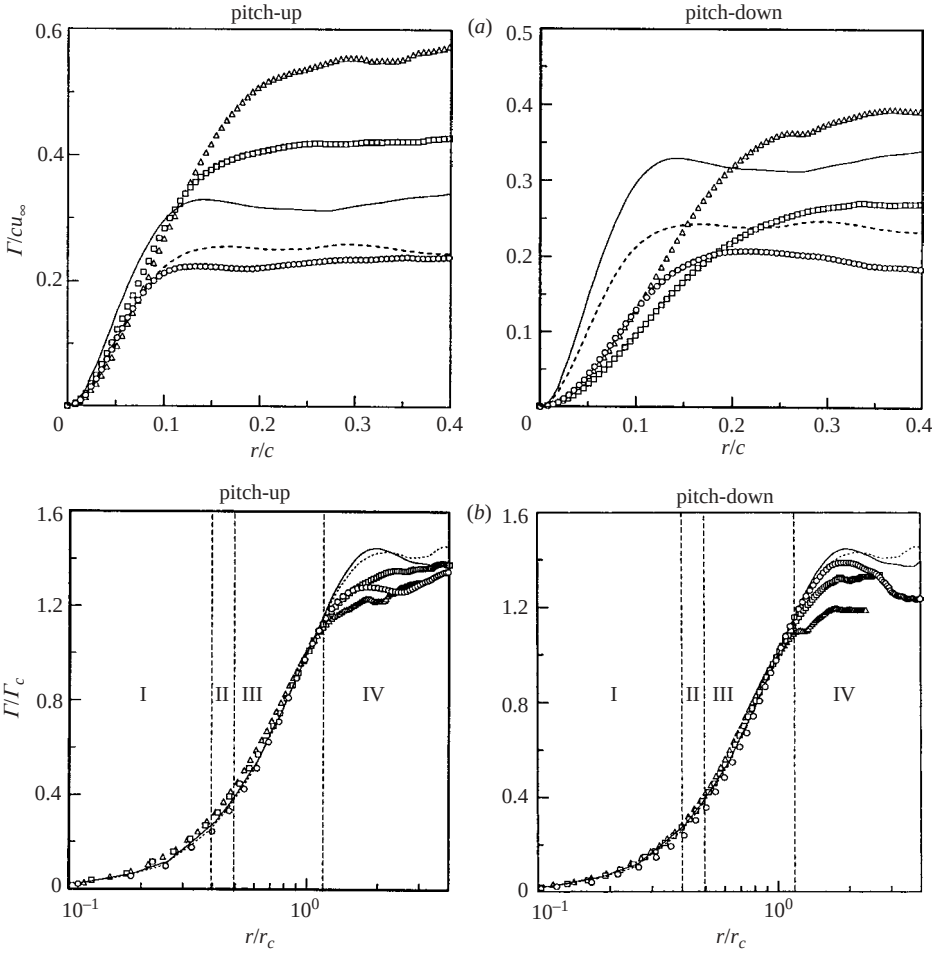

FIGURE 14(*a*, *b*). For caption see facing page.

Finally, the dynamic-loop of the phase-locked ensemble-averaged C_{Di} was also computed (figure 14*e*). Similar to the observed trend in Γ, the values of C_{Di} were found to increase linearly with α up to $\alpha_u \approx 20°$ during pitch-up (with a local maximum $C_{Di} = 0.013$), followed by a decrease for $\alpha_u = 20°$ to $\alpha_d = 20°$. The C_{Di}, however, remained basically unchanged ($C_{Di} = 0.0025$) during the pitch-down flow reattachment process ($\alpha_d = 20°$–$13°$). The rate of increase of C_{Di} per unit α was much higher during pitch-up than during pitch-down. The minima in the C_{Di} loops generally occurred when the circulation was weakest, or at smallest α. The maxima in the C_{Di} loops occurred when the tip vortex was strongest which, notably, was not at α_{max}.

The spatial-temporal variation of the non-dimensional critical vortex flow quantities and C_{Di} with the downstream distance ($x/c = 0.5$–3.0) over an oscillation cycle is illustrated in figure 15. $v_{\theta peak}$ and ζ_{peak} (r_c and r_o) had higher (lower) magnitudes during pitch-up (pitch-down) than during pitch-down (pitch-up), regardless of x/c. The peak tangential velocity was, however, found to decrease with the downstream distance (for $x/c > 1.5$) and increase with α (figure 15*a*). No noticeable variation in r_c and r_o was observed with increasing x/c during pitch-up (figures 15*b* and 15*c*); the

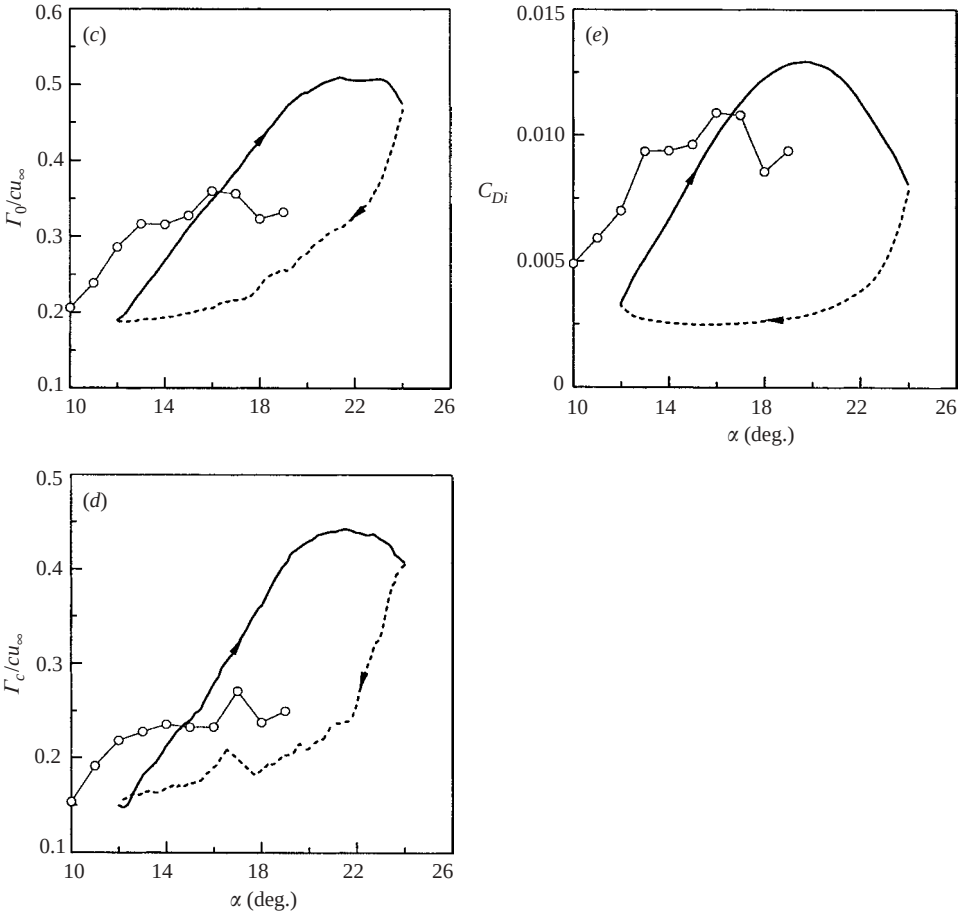

FIGURE 14. Vortex strength and lift-induced drag coefficient for $\alpha(t) = 18° + 6° \sin \omega t$, $\kappa = 0.09$ at $x/c = 1.0$. (*a*) $\Gamma(r)/u_\infty c$, (*b*) Γ/Γ_c, (*c*) $\Gamma_o/u_\infty c$, (*d*) $\Gamma_c/u_\infty c$, and (*e*) C_{Di}. Pitch-up: ○, $\alpha_u = 13°$; □, $\alpha_u = 18°$; Δ, $\alpha_u = 22°$. Pitch-down: ○, $\alpha_d = 13°$; □, $\alpha_d = 16°$; Δ, $\alpha_d = 19°$. Static wing: ——, $\alpha = 13°$; · · · · · ·, $\alpha = 18°$. I: inner-core region, II: buffer region, III: logarithmic region, and IV: outer region.

vortex size was found to increase with the downstream distance during pitch-down. The degree of asymmetry, or hysteresis, in $v_{\theta peak}$ (r_c and r_o) was found to be a weaker (stronger) function of x/c. The magnitudes of the core vorticity were insensitive to x/c during pitch-down while decreasing rather significantly with the downstream distance during pitch-up (figure 15*d*). For $x/c > 1.0$, the axial velocity distributions were wake-like during the entire oscillation cycle. Both Γ_c and Γ_o were relatively insensitive to x/c, especially during the pitch-up motion (figures 15*e* and 15*f*). Figure 15(*g*) indicates that a significant increase in C_{Di} during pitch-up at $x/c = 0.5$ was observed. Only small variation in C_{Di} with x/c was noticed for $x/c > 0.5$.

3.2.3. *Effects of mean angle of attack*

The influence of the maximum incidence α_{max} (= 14°, 20° and 24° corresponding to the attached-flow, and the light- and deep-stall oscillation cases, respectively) on the tip vortex was also investigated by varying the mean angle of attack α_m (= 8°, 14° and 18°), while keeping the amplitude $\Delta\alpha = 6°$ and $\kappa = 0.09$ constant. The light-stall

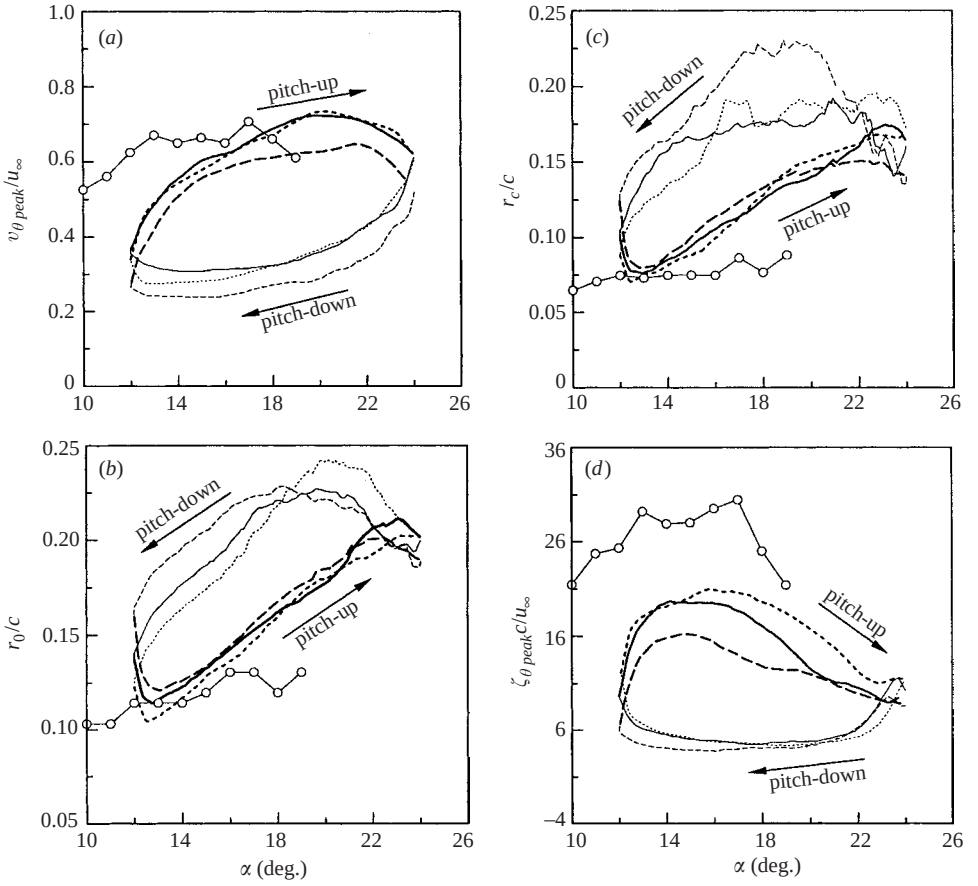

FIGURE 15(*a–d*). For caption see facing page.

oscillation case (with $\alpha_m = 14^\circ$ and $\alpha_{max} = 20^\circ$) is especially interesting, because α_{max} was 5° above α_{ss}, and yet the airfoil never stalled in the dynamic sense. For a light-stalled airfoil, the airfoil stalled from the trailing edge, compared to the leading-edge stall of deep-stall oscillations (Lee & Gerontakos 2004). A vortex-like disturbance, in the leading-edge region, was formed immediately after the turbulent breakdown (following the end of upstream propagation of a flow reversal) as the airfoil continued to pitch up. This disturbance, however, did not have time to grow and was disrupted prematurely as soon as the airfoil pitched through α_{max}. Details of the vortex flow structures at $\alpha_u = \alpha_d = 13^\circ$, 18° and 20° for a NACA 0015 wing oscillated with $\alpha(t) = 14^\circ + 6^\circ \sin \omega t$ and $\kappa = 0.18$ at $x/c = 1$ are presented in figure 17.

Figure 16 shows that the tip vortex was more axisymmetric and less diffusive for $\alpha_u \leqslant 17^\circ$ compared to a static wing, during pitch-up. For $\alpha_u = 18^\circ$–19°, the vortex appeared to have lowered ζ and circulation, attributed to the entrainment and roll-up of the turbulent recirculation flow from the 'vortex-like disturbance'. At $\alpha_u = 20^\circ$ to $\alpha_d = 19^\circ$, the disruption of the vortex-like disturbance on the suction side which fed into the vortex led to a disorganized vortex of increased vortex strength. The separated flow began to reattach onto the wing upper surface for $\alpha_d = 19^\circ$ to 12° and resulted in the re-establishment of an organized tip vortex. For $\alpha_d = 12^\circ$ to 8°, the attached boundary-layer flow rendered a concentrated and axisymmetric vortex

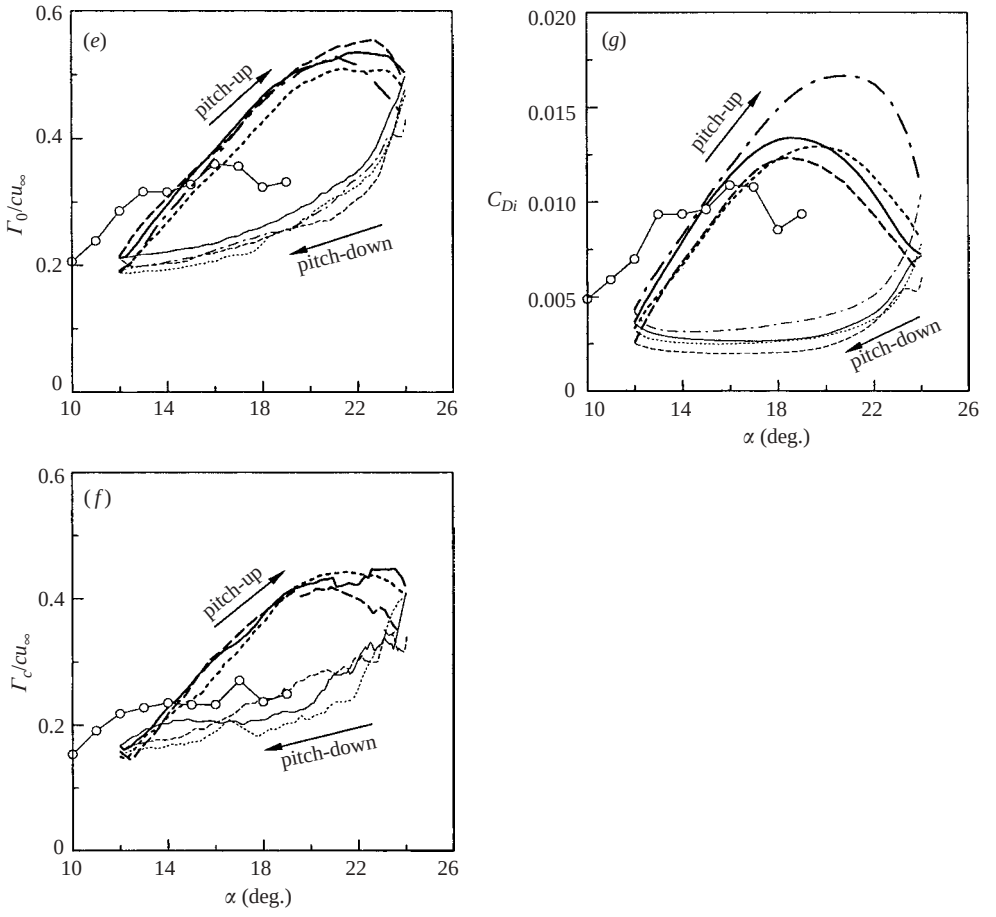

FIGURE 15. Variation of vortex flow quantities and C_{Di} with x/c for $\alpha(t) = 18° + 6° \sin \omega t$, $\kappa = 0.09$. (*a*)$v_{\theta peak}/u_\infty$, (*b*) r_o/c, (*c*) r_c/c, (*d*) $\zeta_{peak}c/u_\infty$, (*e*) $\Gamma_o/u_\infty c$, (*f*) $\Gamma_c/u_\infty c$, and (*g*) C_{Di}. -·-·-, $x/c = 0.5$; ·····, $x/c = 1.0$; ——, $x/c = 1.5$; ----, $x/c = 2.5$. ○, static wing.

resembling that of a static wing at the same α. In addition, the axial flow was always wake-like during pitch-up while it contained islands of wake- and jet-like flow during pitch-down. The present measurements also indicate that the tangential velocity across the vortex and the core vorticity were much larger during pitch-up than during pitch-down (figures 17*a* and 17*b*). The tip vortex was far more organized and the flow was nearly axisymmetric for the major part of the vortex during pitch-up. This difference is primarily because during the pitch-up motion the boundary layer over the inboard regions of the wing tended to remain attached to the surface resulting in a wake that was less turbulent and better organized. This organized vortical layer rolled up into the tip vortex resulting a corresponding well-organized vortex. On the other hand, the flow over the wing during the pitch-down motion was likely to detach itself from the surface at the larger values of α and reattach at smaller values. This resulted in a more turbulent and disorganized wake that rolled into the tip vortex, as can be seen from the results for $\alpha_d = 10°$ during pitch–down. No significant difference in the vortex size and vortex trajectory, compared to a static wing, was observed during the entire oscillation cycle (figures 17*d*–17*e*). In addition, a small hysteresis in the dynamic Γ

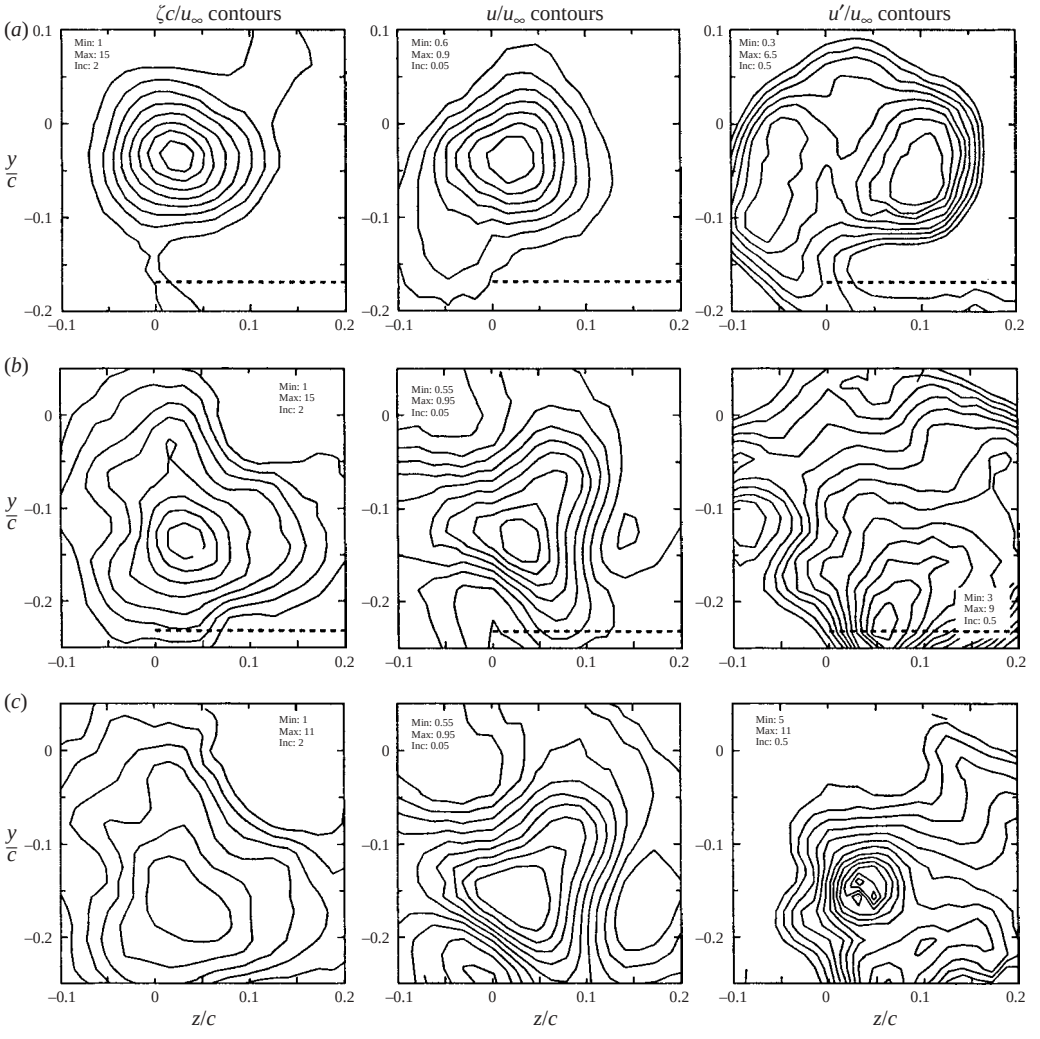

FIGURE 16(*a–c*). For caption see facing page.

and C_{Di} loops existed between the pitch-up and pitch-down motion (figures 17*f*–17*h*), similar to the attached-flow oscillation, with the pitch-up values lower than those during pitch-down.

The effects of α_m on the dynamic loops of the critical vortex flow quantities and C_{Di} at $x/c = 1.0$ and $\kappa = 0.09$ are presented in figure 18. The pronounced variation of the critical vortex flow quantities and C_{Di} with α_m, or α_{max}, during one cycle of oscillation is evident. The values of $v_{\theta peak}$, ζ_{peak} and u_c were generally smaller than the static-wing values (figures 18*a*–18*c*); the magnitudes were higher during pitch-down than during pitch-up for the attached-flow oscillation. For light- and deep-stall oscillations higher values, however, were observed during pitch-up than during pitch-down. The vortex size basically remained similar to that of a static wing for a NACA 0015 wing oscillated within or through α_{ss} (figures 18*d* and 18*e*), but increased significantly above the static-wing values for deep-stall oscillations. The vortex size was larger during pitch-down than during pitch-up for deep-stall oscillations at $\kappa = 0.09$. The dynamic Γ and C_{Di} values were found to increase with $\alpha(t)$ and had pitch-up values higher

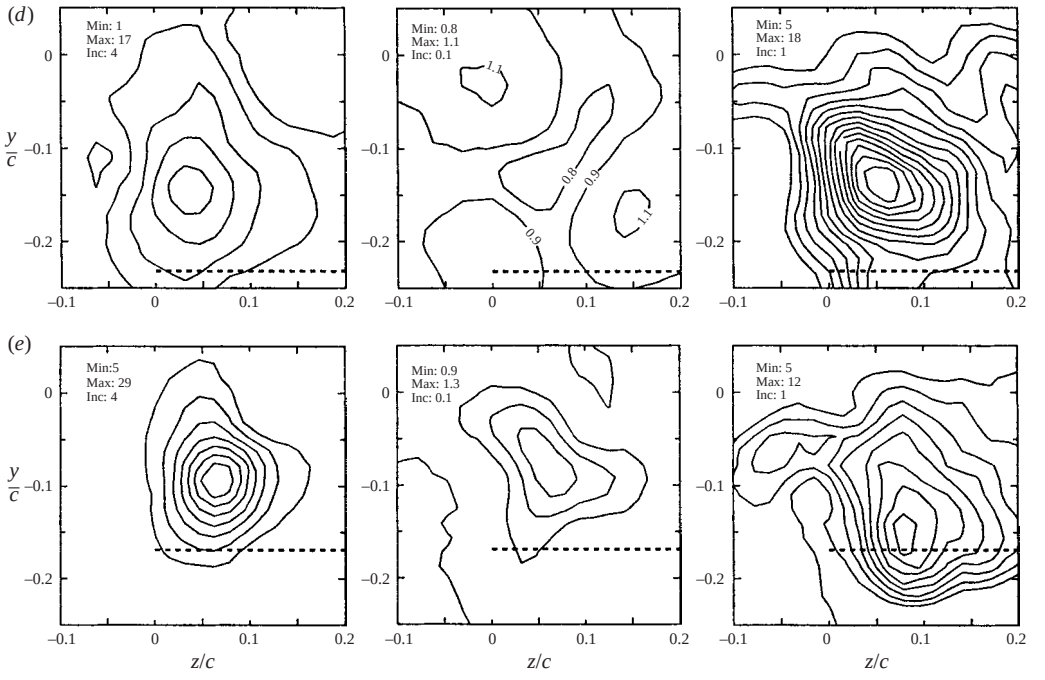

FIGURE 16. Typical phase-locked ensemble-averaged vortex flow structures at $\alpha_u = \alpha_d = 13°$, 18° and 20° for $\alpha(t) = 14° + 6° \sin \omega t$ and $\kappa = 0.18$ with $x/c = 1.0$. Numerical values denote $\zeta c/u_\infty$, u/u_∞, and u'/u_∞ levels with constant increments of 2, 1, and 4, respectively. (*a*) $\alpha_u = 13°$, (*b*) $\alpha_u = 18°$, (*c*) $\alpha_u = 20°$, (*d*) $\alpha_d = 18°$, (*e*) $\alpha_d = 13°$.

than those associated with the pitch-down motion (except the $\alpha_m = 8°$ attached-flow case; figures 18*f*–18*h*).

4. Conclusions

The flow structure and the lift-induced drag of a tip vortex generated by both a static and an oscillating NACA 0015 wing were investigated at $Re = 1.86 \times 10^5$. The following brief conclusions were drawn.

For a static wing, the circulation of the vortex reached a peak value at $x/c = 0.05$ and remained virtually unchanged for $x/c > 0.3$. For $x/c = 0.5$ to 2, the nearly axisymmetric tip vortex accounted for 75 % of the bound circulation. The normalized near-field circulation within the inner region of the nearly axisymmetric tip vortex exhibited a self-similar structure, which was insensitive to the airfoil incidence. As α was increased, the increase in the lift force also resulted in a basically linear increase in the vortex strength up to α_{ss}. The variation of $v_{\theta max}$, ζ_{max} and u_c with α followed trends similar to the circulation. The decay (growth) of the peak tangential velocity (core radius) with x/c was small. Depending on α, the axial flow showed islands of wake- and jet-like velocity distributions. Also, for an axisymmetric vortex in the near field behind a static wing, Γ_c/Γ_o was a constant ratio of 0.73 accompanied by r_c/r_o of 0.64.

For attached-flow oscillations, many of the vortex flow features are qualitatively similar to the tip vortex behind a static wing. The oscillating wing produced a less concentrated vortex of similar diameter and had a larger radial gradient in circulation strength, compared to a static wing. The axial velocity distribution across the vortex

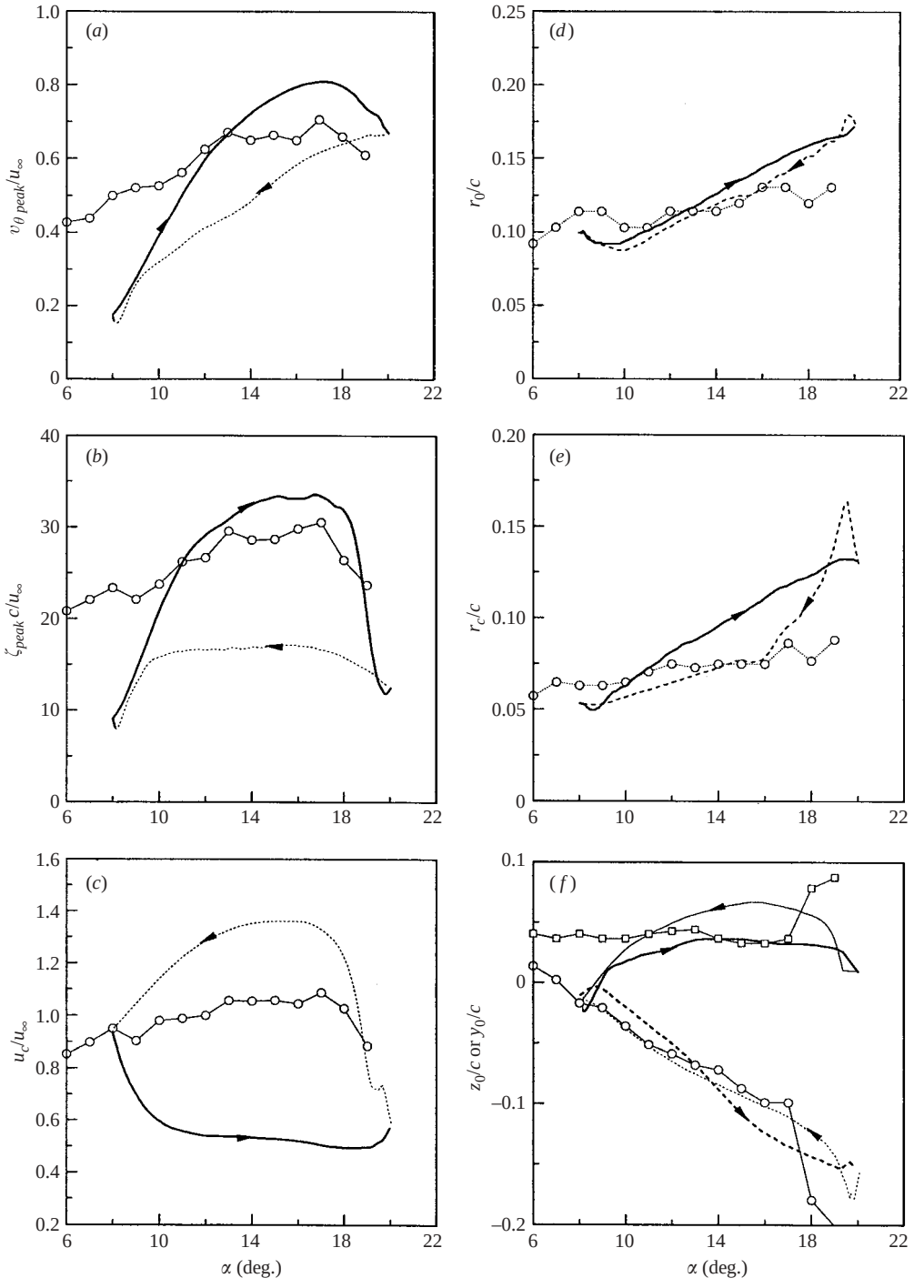

FIGURE 17(*a–f*). For caption see facing page.

varied drastically from a wake-like to a jet-like behaviour during the oscillation cycle. The peak values of the critical vortex flow quantities, including the vortex strength and the lift-induced drag, were progressively higher during pitch-down than during

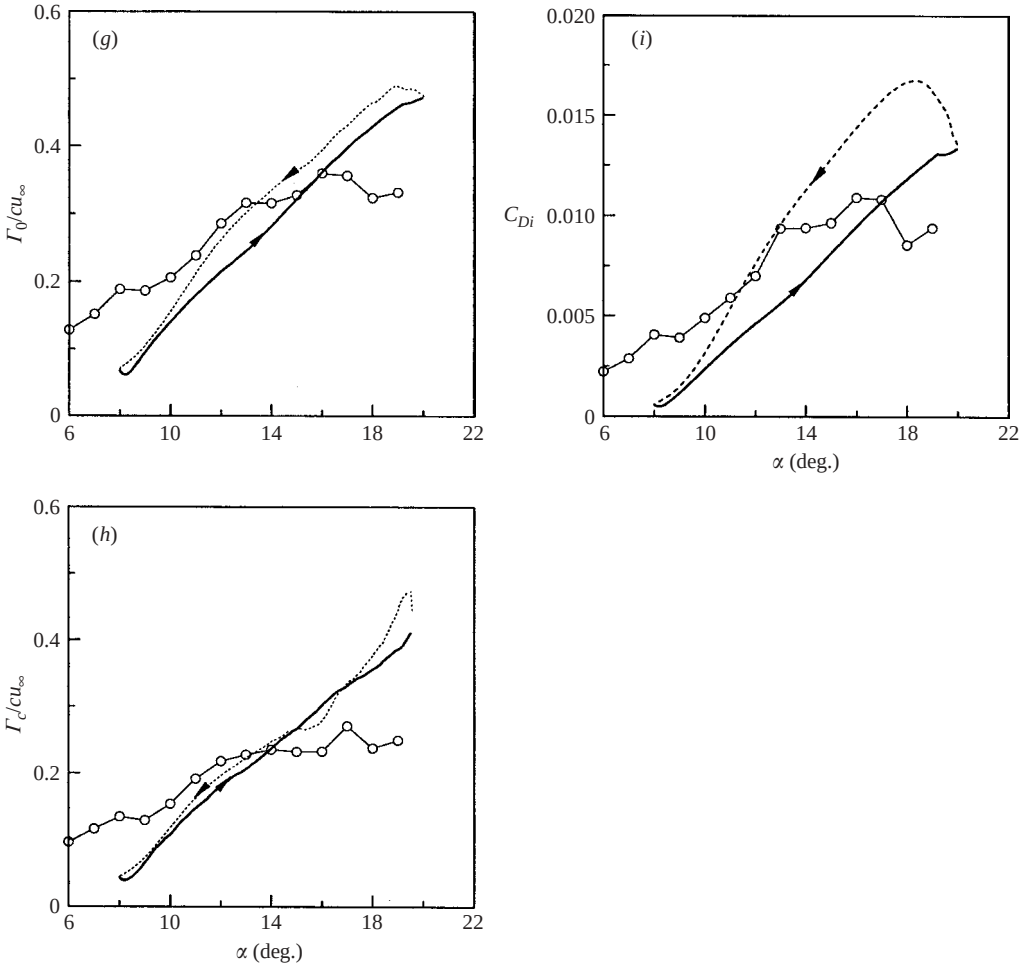

FIGURE 17. Dynamic loops of critical vortex flow quantities and C_{Di} over an oscillation cycle for $\alpha(t) = 14^\circ + 6^\circ \sin \omega t$ and $\kappa = 0.18$ at $x/c = 1.0$. (*a*) $v_{\theta peak}/u_\infty$, (*b*) $\zeta_{peak} c/u_\infty$, (*c*) u_c/u_∞, (*d*) r_o/c, (*e*) r_c/c, (*f*) vortex trajectory (z_o/c: □, static wing; ——, oscillating wing. y_o/c: ○, static wing; · · · · · ·, oscillating wing), (*g*) $\Gamma_o/u_\infty c$, (*h*) $\Gamma_c/u_\infty c$, and (*i*) C_{Di}. ——, pitch-up; · · · · · ·, pitch-down. ○, static wing.

pitch-up, and increased with α. The level of hysteresis increased slightly with κ. Similar to the case of a static wing, when a decaying vortex maintained geometric similarity, Γ_c/Γ_o and r_c/r_o were constant. The self-similarity in the normalized circulation within the inner region of the vortex also persisted. Similar vortex flow characteristics, compared to attached-flow oscillations, were also observed for a wing undergoing light-stall oscillations. The tip vortex, however, appeared to have reduced ζ and circulation due to the entrainment and roll-up of the turbulent recirculation flow from the 'vortex-like disturbance' during pitch-down. A rather disorganized vortex of reduced strength was observed as soon as the wing pitched through α_{max}, as a result of the disruption of the vortex-like disturbance on the suction side which fed into the vortex. The tip vortex became organized as the separated flow began to reattach onto the wing upper surface for the rest of the pitch-down flow-reattachment process.

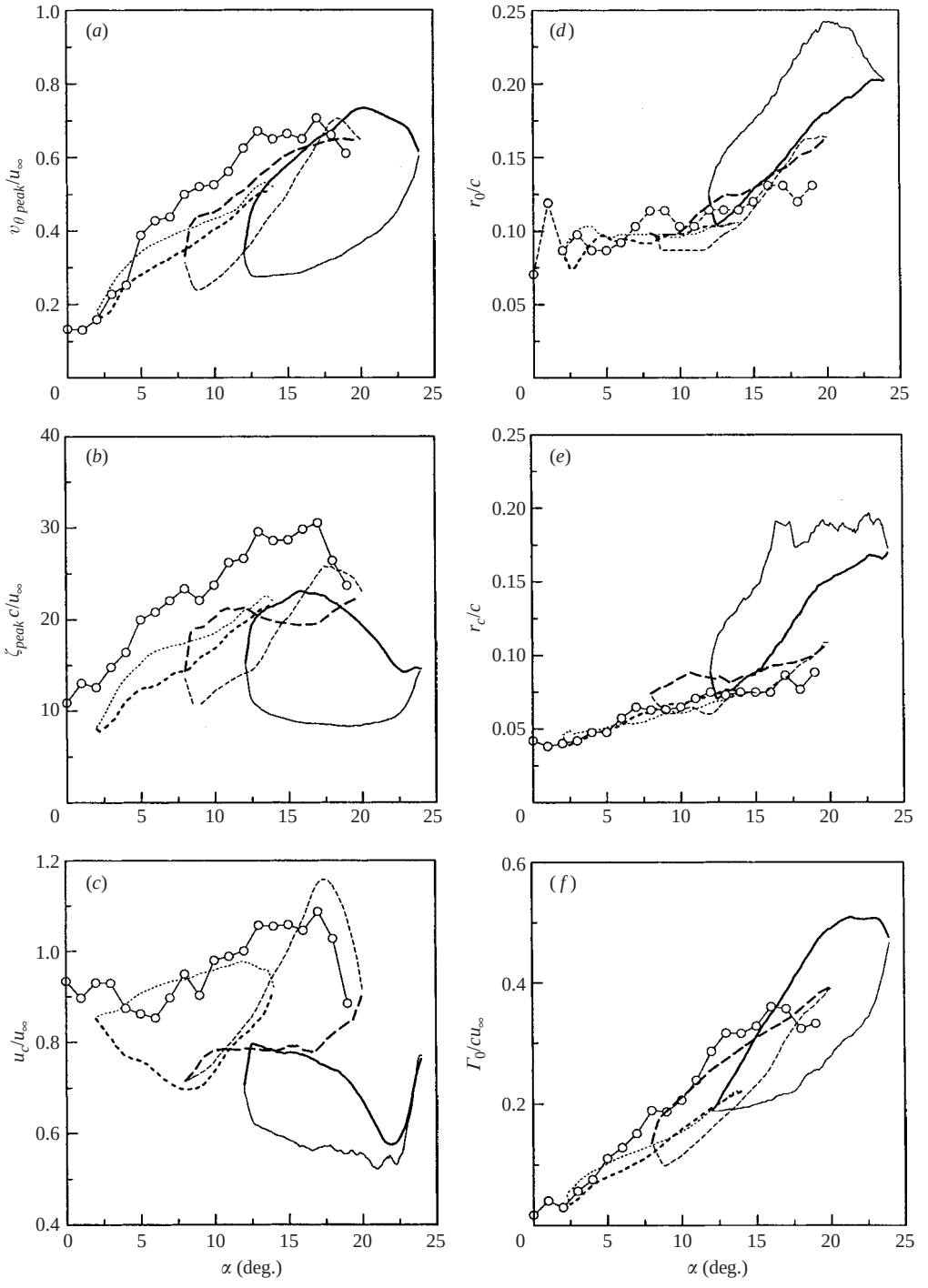

FIGURE 18(*a–f*). For caption see facing page.

For a wing subjected to deep-stall oscillations, the wing oscillations imposed a strong discrepancy in contour shapes and magnitudes between the pitch-up and pitch-down phases of the oscillation cycle. The vortex was more organized and axisymmetric

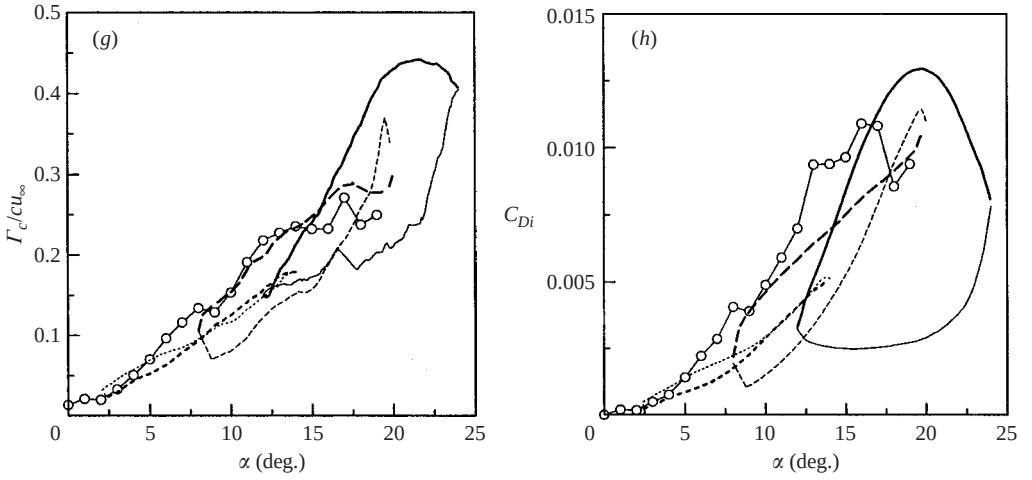

FIGURE 18. Dynamic loops of the critical vortex flow quantities and C_{Di} over an oscillation cycle at $x/c = 1.0$, $\kappa = 0.18$, and $\Delta\alpha = 6°$. (*a*) $v_{\theta peak}/u_\infty$, (*b*) $\zeta_{peak}c/u_\infty$, (*c*) u_c/u_∞, (*d*) r_o/c, (*e*) r_c/c, (*f*) $\Gamma_o/u_\infty c$, (*g*) $\Gamma_c/u_\infty c$, and (*h*) C_{Di}. ·····, $\alpha_m = 8°$; ----, $\alpha_m = 14°$; ——, $\alpha_m = 18°$. ○, static values. Thick line: pitch-up; thin line: pitch-down.

(for $x/c > 0.5$) during pitch-up than during pitch-down, except in the vicinity of α_{max}. This difference was primarily because during pitch-up the boundary layer over the inboard regions of the wing tended to remain attached to the surface resulting in a wake that was less turbulent and better organized, while during pitch-down the flow was largely separated as a result of the LEV detachment. The tangential velocity and circulation increased with α and decreased slightly with x/c, and had higher magnitudes during pitch-up than during pitch-down. The vortex size increased with α and was larger during pitch-down than during pitch-up. The vortex size was also observed to increase with x/c during pitch-down while remaining virtually unchanged with x/c during pitch-up. The axial velocity distribution across the vortex was always wake-like during the oscillation cycle and decreased with α, followed by a significant increase and decrease in the vicinity of α_{max}. The normalized circulation within the inner region of the nearly axisymmetric tip vortex also exhibited a self-similar structure, similar to that of a static wing, and was insensitive to κ. Both circulation and C_{Di} had higher magnitudes during pitch-up than during pitch-down, and varied insignificantly with x/c and increased with κ.

This work was supported by the Natural Sciences and Engineering Research Council (NSERC) of Canada.

REFERENCES

BATCHELOR, G. K. 1964 Axial flow in trailing line vortices. *J. Fluid Mech.* **20**, 645–658.

BIRCH, D. & LEE, T. 2004 Structure and induced drag of a tip vortex. *J. Aircraft* **41**, 1138–1145.

BRUNE, G. W. 1994 Quantitative low-speed wake surveys. *J. Aircraft* **31**, 249–255.

CARR, L. W., MCALISTER, K. W. & MCCROSKEY, W. J. 1977 Analysis of the development of dynamic stall based on oscillating airfoil experiments. *NASA TN* D-8382.

CHANDRASEKHARA, M. S. & CARR, L. W. 1990 Flow visualization studies of the Mach number effects on dynamic stall of an oscillating airfoil. *J. Aircraft* **27**, 516–522.

CHANG, J. W. & PARK, S. O. 2000 Measurement in the tip vortex roll-up region of an oscillating wing. *AIAA J.* **38**, 1092–1095.

Chow, J. S., Zilliac, G. G. & Bradshaws, P. 1997 Mean and turbulence measurements in the near field of a wingtip vortex. *AIAA J.* **35**, 1561–1567.

Corsiglia, V. R., Schwind, R. G. & Chigier, N. A. 1973 Rapid scanning, three-dimensional hot-wire anemometer surveys of wing-tip vortices. *J. Aircraft* **10**, 752–757.

Crow, S. C. 1979 Stability theory for a pair of trailing vortices. *AIAA J.* **8**, 2172–2179.

Devenport, W. J., Rife, M. C., Liapis, S. I. & Follin, G. J. 1996 The structure and development of a wing-tip vortex. *J. Fluid Mech.* **312**, 67–106.

Ericsson, L. E. & Reding, J. P. 1988 Fluid mechanics of dynamic stall. Part I. Unsteady flow concept. *J. Fluids Struc.* **2**, 1–33.

Francis, M. S. & Kennedy, D. A. 1979 Formation of a trailing vortex. *J. Aircraft* **15**, 148–154.

Francis, T. B. & Katz, J. 1988 Observations on the development of a tip vortex on a rectangular hydrofoil. *Trans. ASME: J. Fluids Engng* **110**, 208–215.

Freymuth, P., Finaish, F. & Bank, W. 1985 Visualization of wing-tip vortices in accelerating and steady flow. *J. Aircraft* **23**, 730–733.

Gerz, T. & Holzapfel, F. 1999 Wing-tip vortices, turbulence, and the distribution of emissions. *AIAA J.* **37**, 1270–1276.

Glauert, H. 1926 *The Elements of Aerofoil and Airscrew Theory*. Cambridge University Press.

Green, S. I. & Acosta, A. J. 1991 Unsteady flow in trailing vortices. *J. Fluid Mech.* **227**, 107–134.

Hoffmann, E. R. & Joubert, P. N. 1963 Turbulent line vortices. *J. Fluid Mech.* **16**, 395–411.

Johnson, W. & Ham, N. D. 1972 On the mechanism of dynamic stall. *J. Am. Helicopter Soc.* 36–45.

Jumper, E. J., Dimmick, R. L. & Allatre, A. J. S. 1989 The effect of pitch location on dynamic stall. *Trans. ASME: J. Fluids Engng* **111**, 256–262.

Ko, S. & Mccroskey, W. J. 1997 Computations of unsteady separating flows over an oscillating airfoil. *AIAA J.* **35**, 1235–1238.

Kusunose, K. 1997 Development of a universal wake survey data analysis code. *AIAA Paper* 97-2294.

Lamb, H. 1945 *Hydrodynamics*, 6th edn, p. 592 Dover.

Lee, T. & Basu, S. 1998 Measurement of unsteady boundary layer developed on an oscillating airfoil using multiple hot-film sensors. *Exps. Fluids* **25**, 108–117.

Lee, T. & Gerontakos, P. 2004 Investigation of flow over an oscillating airfoil. *J. Fluid Mech.* **512**, 313–341.

McAlister, K. W. & Takahashi, R. K. 1991 NACA 0015 wing pressure and trailing vortex measurements. *NASA TP*-3151.

McCroskey, W. J. 1982 Unsteady airfoils. *Annu. Rev. Fluid Mech.* **14**, 285–311.

McCroskey, W. J., McAllister, K. W., Carr, L. W., Pucci, S. L., Lamber, O. & Indergrand, R. F. 1981 Dynamic stall on advanced airfoil sections. *J. Am. Helicopter Soc.* **26**, 40–50.

McCroskey, W. J., Carr, L. W. & McAlister, K. W. 1976 Dynamic stall experiments on oscillating airfoils. *AIAA J.* **14**, 57–63.

McCroskey, W. J. & Philippe, J. J. 1975 Unsteady viscous flow on oscillating airfoils. *AIAA J.* **13**, 71–79.

Maskell, E. 1973 Progress towards a method for the measurement of the components of the drag of a wing of finite span. *RAE Tech. Rep.* 72232.

Mayer, E. W. & Powell, K. G. 1992 Similarity solutions for viscous vortex cores. *J. Fluid Mech.* **238**, 487–507.

Moore, D. W. 1974 Numerical study of the roll-up of a finite vortex sheet. *J. Fluid Mech.* **65**, 225–235.

Moore, D. W. & Saffman, P. G. 1973 Axial flow in laminar trailing vortices. *Proc. R. Soc. Lond.* A **333**, 491–508.

Naik, D. A. & Ostowari, C. 1990 Effects of nonplanar wing forms on a wing. *J. Aircraft* **27**, 117–122.

Panda, J. & Zaman, B. M. Q. 1994 Experimental investigation of the flow field of an oscillating airfoil and estimation of lift from wake surveys. *J. Fluid Mech.* **265**, 65–95.

Phillips, W. R. C. 1981 The turbulent trailing vortex during roll-up. *J. Fluid Mech.* **105**, 451–467.

Ramaprian, B. R. & Zheyg, Y. 1997 Measurements in rollup region of the tip vortex from a rectangular wing. *AIAA J.* **35**, 1837–1843.

Ramaprian, B. R. & Zheng, Y. 1998 Near field of the tip vortex behind an oscillating rectangular wing. *AIAA J.* **36**, 1263–1269.

Rossow, V. J. 1973 On the inviscid rolled-up structure of lift-generated vortices. *J. Aircraft* **10**, 647–650.

SchreckC, S., Faller, W. & Heliln, H. 1994 Pitch rate and Reynolds number effect on unsteady boundary layer transition and separation. *AIAA Paper* 94-2256.

Shekarriz, A., Fu, T. C., Katz, J., & Huang, T. T. 1993 Near-field behaviour of a tip vortex. *AIAA J.* **31**, 112–118.

Spalart, P. R. 1998 Airplane trailing vortices. *Annu. Rev. Fluid Mech.* **30**, 107–138.

Srinivassan, G. R., Ekaterinaris, J. A. & Mccroskey, W. J. 1993 Dynamic stall of an oscillating wing. Part 1: Evaluation of turbulence models. *AIAA Paper* 93-3403.

Wenger, C. W. & Devenport, W. J. 1999 Seven-hole pressure probe calibration utilizing look-up error tables. *AIAA J.* **37**, 675–679.

Williams, G. M. 1974 Viscous modeling of wing-generated trailing vortices. *Aero. Q.* **25**, 143–154.